A. Romei, G. Persico (2021) *Computational fluid-dynamic modelling of two-phase compressible flows of carbon dioxide in supercritical conditions*, Applied Thermal Engineering, Vol. 190, 116816 (20 pages), doi: 10.1016/j.applthermaleng.2021.116816

Computational fluid-dynamic modeling of two-phase compressible flows of carbon dioxide in supercritical conditions

Alessandro Romei, Giacomo Persico*

Laboratory of Fluid Machines
Energy Department, Politecnico di Milano
Via Lambruschini 4, 20156 Milano, Italy

Abstract

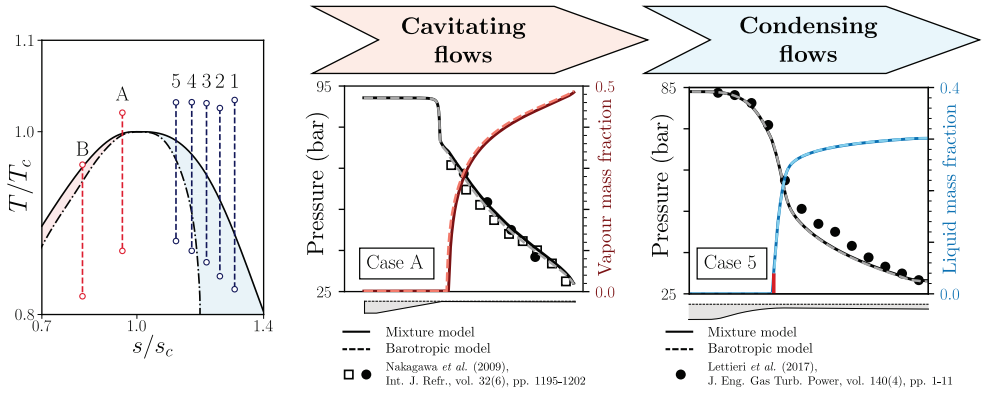

Compressible two-phase flows of carbon dioxide in supercritical thermodynamic conditions are encountered in many applications, e.g. ejectors for refrigeration and compressors for power production and carbon capture and sequestration to name a few. Alongside the phase change, transonic/supersonic flow regimes and real-gas effects also add additional complexities in the simulations of such flows. In this work, we investigate cavitating and condensing flows of carbon dioxide via numerical simulations based on the two-fluid concept, applying both a mixture model and a barotropic model. In the mixture model, the phase change is modelled with an extra transport equation for the mass of the dispersed phase and a source term introduced via a penalty formulation. The barotropic model reproduces the pressure-density relation of the mixture along the upstream isentrope. Both the models assume thermodynamic and mechanical equilibrium between phases and exclude meta-stability effects. All results are compared against experimental data taken from literature and the main numerical issues of the models are discussed in detail. The agreement between the simulations and the experiments is remarkable even though suggesting a further margin of improvement in the physical modeling. Finally, we show that the barotropic model yields comparable predictions of the expansion processes at a lower computational cost and with an improved solver robustness.

Keywords: carbon dioxide, two-phase flows, non-ideal effects, supersonic flows.

Preprint submitted to Applied Thermal Engineering

1. Introduction

Carbon dioxide (CO_2) is not only a greenhouse gas. Thanks to its low toxicity and its thermal stability for wide ranges of pressure and temperature, CO_2 (also known as R744 in the refrigeration field) is also attracting scientific research efforts and R&D investments to enable its usage as working fluid for energy systems and process engineering. Several alternative and novel energy technologies are presently based on the application of CO_2, e.g. refrigeration systems [1, 2] and closed power cycles [3, 4, 5, 6] to name a few. These technologies share a specific technical issue: in at least one component of the system, CO_2 evolves in thermodynamic states close to the critical point.

Depending on the entropy level of the intake supercritical condition, the phase transition might lead to the formation of either vapour (when $s < s_c$) or liquid (when $s > s_c$); in other words, expanding from a general supercritical state either cavitation (liquid $\mapsto$ vapour) or condensation (vapour $\mapsto$ liquid) can take place in supercritical carbon dioxide (sCO_2) flow components. With reference to the flow devices listed above, ejectors for refrigeration typically operate for $s < s_c$, while compressors for CCS operate for $s > s_c$; conversely, compressors for closed power cycles can be run in both the conditions, depending on the cycle configuration, the thermodynamic optimization, and the full-/part-load strategy of the plant. In all these flow devices the phase transition occurs within streams of high-speed fluid; the available experiments (see, for example, the visualization published in [7]) indicate that in such flow configurations the new phase (composed by either droplets or bubbles) appears dispersed into the main one, without evident interfaces between the phases. The onset of a dispersed phase is typically associated to a sudden drop of the speed of sound, which is comparably lower than that of the fluid in either of the saturated conditions. As a result, the onset of two-phase flows is associated to a sudden increase of the Mach number of the stream, promoting the establishment of supersonic flows, shock waves, and choking with respect to single-phase flows of the same fluid [8]. In this context, a proper computational modeling of cavitation and condensation phenomena in sCO_2 compressible flows, and their subsequent implications on the flow morphology and on the thermodynamics of the process, is crucial for the design of sCO_2 devices and, ultimately, for the technical feasibility and market penetration of the entire sCO_2 energy technology.

Two-phase flows were object of theoretical, computational and experimental studies in the last decades; historically, the vast majority of these studies was focused on water for cavitation in pumps [9] and valves [10, 11], on cryogenic fluids for rocket turbopumps [12, 13] and on steam for condensation in turbines [14, 15, 16]. The outcome of these studies is best summarized, to the authors' knowledge, in the excellent book of Brennen [17], which provides a rigorous and comprehensive presentation of two-phase flows, with emphasis on both the physical and modeling perspectives. With reference to Brennen's classification, the

*Corresponding author
Email address: giacomo.persico@polimi.it (Giacomo Persico)

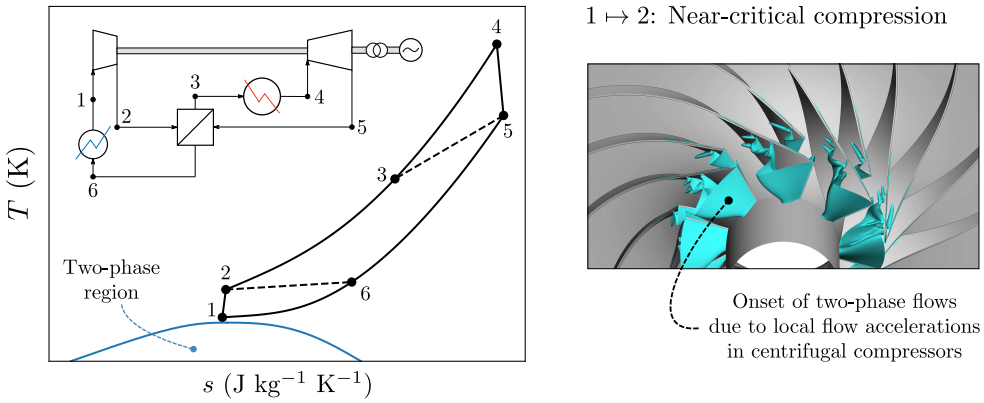

Figure 1:

so-called *two-fluid model* appears to be the most computational-effective formulation to model the dispersed phase transitions of interest in this work. In the two-fluid model, the dispersed phase is considered mixed from an Eulerian perspective with the main phase in a unique continuous fluid, whose mean properties are defined on the basis of proper volume or mass averages of the corresponding single-phase properties. Even within this modeling framework, several alternative sub-models were proposed in the scientific literature to treat the generation of the dispersed phase and the interaction between the phases.

The typical short time-scale of the process might allow the supercritical fluid to expand below the saturation limit without incurring in a phase change, reaching the so-called meta-stable state. Meta-stable states might exist within limited thermodynamic regions, comprised between the saturation curve (representative of the phase transition under thermodynamic equilibrium) and the spinodal curve (limit of the meta-stable equilibrium). Experiments for wet steam [18] and, recently, for sCO_2 [7] indicate that in high-speed flows the transition occurs delayed with respect to the saturation line, thus proving the existence of meta-stable states, though in limited regions of the flow. When the two phases are established, velocity and temperature differences might arise between the phases, promoting mechanical and/or thermal non-equilibrium. De Lorenzo *et al.* [19] reviewed the most relevant two-fluid models, classified them with respect to the character of non-equilibrium phenomena to be represented in the solution, and proposed a class of novel one-dimensional analytic solutions of two-phase flows in nozzles.

Such rich scientific background allows us to provide a classification of the most relevant models available for the prediction of cavitating/condensing high-speed flows, which could also be applied in presence of sCO_2 flows:

- the *homogeneous equilibrium model* (HEM), which excludes meta-stable states and assumes mechanical and thermal equilibrium between the phases;

- the *non-homogeneous equilibrium model* (NEM), which excludes meta-stable states and assumes thermal equilibrium between the phases, but allows for the existence of a relative velocity between the two phases;
- the *homogeneous frozen model* (HFM), which excludes meta-stable states and assumes mechanical equilibrium, but neglects the heat exchange between the phases;
- the *delayed equilibrium model* (DEM), which allows for the existence of meta-stable states (by considering a third phase, besides the saturated liquid and vapour, composed by the supersatured supercritical fluid), and only considers mechanical equilibrium between the phases.

Brennen [17] and De Lorenzo *el al.* [19] successfully applied these models in simple geometric configurations like ducts and nozzles, where quasi-one-dimensional analytical solutions provide a technically relevant representation of the flow. However, to pursue the thermofluid-dynamic design of the technical devices of interest for sCO_2 technology, the aforementioned models have to be reformulated in order to be implemented in a multi-dimensional computational fluid-dynamic (CFD) framework. Examples of two-phase models implemented in the frame of CFD tools are reported in [20] and [21], mainly focusing on water cavitation. With respect to such studies, the supercritical condition of CO_2 complicates the thermodynamic modeling of the single phases, besides the inherent complication associated to the phase change. Recently, examples of CFD simulations of two-phase flows of sCO_2 were proposed [22, 23, 24, 25], and compared with experiments performed on either cavitating or condensing flows of sCO_2 in converging-diverging nozzles. However, in none of the aforementioned publications the proposed CFD model is compared to both classes of phase transition.

This paper is structured as follows. At first the computational models are outlined, then the two test-cases are presented. The results of the application of the flow models to, first, cavitating flows and, then, condensing flows are discussed, highlighting modeling issues and computational accuracies. Finally, a critical discussion on the calculation of the speed of sound in presence of cavitating and condensing flows is proposed.

2. Computational framework

In this section, we outline the two computational formulations that will be used throughout this work, highlighting the main modeling assumptions. Both of them stems from the two-fluid concept, but they differ in terms of the thermodynamic treatment and, ultimately, in the way in which the dispersed phase is generated and evolves within the main one. Both the flow models are implemented in the Ansys-Fluent® framework making use of ad-hoc user-defined functions (UDFs).

The first model, named *mixture model* hereinafter, considers the mixture as a whole instead of being composed by two distinct phases. Such flow modeling allows for a drastic simplification in the mathematical

description of the two-phase flow: the classical set of Reynolds-Average Navier-Stokes equations is recovered and formulated in terms of mixture density and mixture centre-of-mass velocity, eventually complemented with constitutive equations to model the relative motion between phases. Analogously, the energy equation is expressed in terms of the mixture enthalpy.

Defining the volumetric fraction of the main or principal phase as α_p and that of the dispersed phase as α_d, the mixture density ρ_m, molecular viscosity μ_m and thermal conductivity κ_m result from the volume-weighted average as follows:

$$\rho_m = \alpha_p \rho_p + \alpha_d \rho_d \tag{1}$$

$$\mu_m = \alpha_p \mu_p + \alpha_d \mu_d \tag{2}$$

$$\kappa_m = \alpha_p \kappa_p + \alpha_d \kappa_d \tag{3}$$

It is recalled that $\alpha_p = 1 - \alpha_d$ for single-component two-phase flow. Any specific thermodynamic quantity of the mixture ψ_m (such as enthalpy, entropy, internal energy, etc...) is instead evaluated using mass-averages, by resorting to the mass fractions of the phases. The mass fractions of the primary and dispersed phases, defined as w_p and w_d respectively, are evaluated as:

$$w_p = \frac{\rho_p}{\rho_m} \alpha_p \tag{4}$$

$$w_d = \frac{\rho_d}{\rho_m} \alpha_d \tag{5}$$

From mass conservation, the two mass fractions sum to unity, i.e. $w_p + w_d = 1$. They are used to determine the general specific mixture quantity ψ_m as follows:

$$\psi_m = w_p \psi_p + w_d \psi_d \tag{6}$$

An additional transport equation for the mass of the dispersed phase describes the generation and the evolution of the dispersed phase. The resulting set of governing equations can effectively track the evolution of averaged properties without resorting to sub-models that account for inner interactions between phases, whose modeling would require a deep knowledge of the interfacial properties [26].

The second model, named *barotropic model* hereinafter, is still based on the two-fluid flow representation and strictly assumes that (i) the phases are in thermal and mechanical equilibrium, and (ii) any thermodynamic/transport property of the mixture Ψ only depends on the pressure, e.g. $\Psi = \Psi(P)$. In general, the generic mixture property for a single-component fluid should depend on two independent thermodynamic quantities, for example $\Psi = \Psi(P, s)$. The barotropic assumption hence implies to neglect the any contribution besides the one of pressure on the quantity of interest; this means, in practice, to neglect the volumetric

thermal expansion of the fluid. However, thanks to the barotropic assumption the equations of motion are decoupled from the energy equation, which does not need to be explicitly resolved. Such model, though highly simplified, is deemed to be particularly relevant for turbocompressor application, since heat transfer is usually negligible in such components and the computational efficiency is crucial for their aerodynamic design and optimization.

2.1. Mixture model

The set of steady-state governing equations for the mixture model reads:

$$\begin{aligned} \nabla \cdot (\rho_m \boldsymbol{v_m}) &= 0 \\ \nabla \cdot (\rho_m \boldsymbol{v_m} \otimes \boldsymbol{v_m}) &= \nabla \cdot (\mathcal{T} + \mathcal{T}_{turb}) - \nabla P_m \\ \nabla \cdot (\rho_m h_m^t \boldsymbol{v_m}) &= -\nabla \cdot (\boldsymbol{q} + \boldsymbol{q}_{turb}) + \nabla \cdot [\boldsymbol{v_m}(\mathcal{T} + \mathcal{T}_{turb})] \\ \nabla \cdot (\alpha_d \rho_d \boldsymbol{v_m}) &= \mathcal{G} \end{aligned} \tag{7}$$

where no slip velocity is considered between phases, i.e. $\boldsymbol{v} = \boldsymbol{v_m} = \boldsymbol{v_p} = \boldsymbol{v_d}$, and equal pressure and temperature is assumed between the phases, i.e. $P = P_m = P_p = P_d$ and $T = T_m = T_p = T_d$, thus imposing thermal and mechanical equilibrium. The shear-stress relationship for an isotropic Newtonian fluid is supplied $\mathcal{T} = \mu_m(\nabla \otimes \boldsymbol{v_m} + (\nabla \otimes \boldsymbol{v_m})^T)$, where the contribution given by the volume viscosity coefficient is neglected in the mixture model implementation by Ansys-Fluent®. The Fourier's law $\boldsymbol{q} = -\kappa_m \nabla T_m$ is used for the heat conduction. The gross effects of turbulence, expressed by the Reynolds stresses $\mathcal{T}_{turb}$ and the turbulent heat transfer $\boldsymbol{q}_{turb}$, are introduced by means of the well-known two-equation $k - \omega$ SST model [27]. It follows that a system consisting in seven partial differential equations has to be solved for a two-dimensional problem.

The last equation of system (7) is the specific feature of the proposed mixture model and its formulation is crucial to obtain smooth numerical convergence and accurate results. The role of this equation is actually to produce a certain amount of mass-flow rate of the dispersed phase (left-hand side of the equation) when the local thermodynamic state resulting from the numerical calculation reaches the condition of phase transition by activating a mass-transfer source term $\mathcal{G}$ (right-hand side of the equation). Several formulations were proposed for this source term (see, for example, Dang *el al.*, [21], Giacomelli *el al.*, [23], Boyds *el al.*, [25]), typically referring to the Hertz-Knudsen physical model [28]. In the present work, we propose a formulation similar to the one used in Hosangadi *el al.* [24] but with a different concept and implementation. We define $\mathcal{G}$ as:

$$\mathcal{G} = \mathrm{sgn}(s_0 - s_c)\, \mathcal{K}\, [P - P_{sat}(T)]\,, \tag{8}$$

which is valid for both $P > P_{sat}(T)$, which implies condensing flows, and for $P < P_{sat}(T)$, which reproduces cavitating flows. Otherwise, $\mathcal{G} = 0$ because there is no phase change.

In our model, $P - P_{sat}(T)$ is the driving force of the phase change: when the local pressure exceeds (goes below) the saturation pressure at the local temperature, condensation (cavitation) locally occurs generating an increase in the mass of the dispersed phase. In this sense, such source term effectively mimics the Hertz-Knudsen model; however, the Hertz-Knudsen model was conceived to represent processes occurring at the microscale, which are not solved in the continuum macroscopic framework of the CFD. Hence, we just retain the general intuition to construct the mathematical model: from the mathematical perspective, this formulation is actually a *penalty* term introduced in the equation to numerically impose the satisfaction of a constraint, i.e. the onset of transition when $P = P_{sat}(T)$. Therefore, the numerical difference $P - P_{sat}(T)$ can be interpreted as a violation of the stable thermodynamic equilibrium and it becomes an artificial effect of the penalty formulation. To control $P - P_{sat}(T)$, and thus recovering an accurate numerical approximation of the two-phase solutions, i.e. $P \approx P_{sat}(T)$, the formulation of $\mathcal{G}$ features the penalty coefficient $\mathcal{K}$ [$\mathrm{s\,m^{-2}}$], which is dimensional and represents the weight of the penalty: the higher the $\mathcal{K}$, the lower $P - P_{sat}(T)$. In the result section, we will show the influence of this parameter on the accuracy of the solutions. It is only anticipated that $\mathcal{K} = \mathcal{O}(10^2 \div 10^3)\,\mathrm{s\,m^{-2}}$ is sufficient to impose that, in the two-phase region of the flow, the solution links the pressure field with the temperature field such that the actual P approximates $P_{sat}(T)$ with a small numerical error ($< 0.5\%$).

It is also worth mentioning that the present interpretation is fundamentally different from that of Dang *et al.* [21], in which the pressure difference is assigned a priori, Hosangadi *et al.* [24], in which the equilibrium condition $P = P_{sat}(T)$ is not recovered in the solution, and Bodys *et al.* [25], in which a reference saturation pressure is defined and the source term monotonically increases along the expansion accordingly.

2.1.1.

A further issue of the mixture model, particularly relevant to sCO_2 application, is the thermodynamic modeling of the supercritical fluid in the single-phase region and of the individual phases in the two-phase region. Due to the near-critical conditions, a generalized thermodynamic description is required. In the present formulation, any generic property Ψ of the single-phase primary phase is expressed as a function of pressure and temperature, i.e. $\Psi_p = \Psi_p(P, T)$. A LUT approach was implemented in Ansys-Fluent® and supplied via a user-defined real-gas model (UDRGM). The value of Ψ_p at a generic pair (P, T) is then computed with a bilinear interpolation between the four closest thermodynamic nodes.

When the primary phase is in equilibrium with the dispersed phase , Ψ_p is only function of the saturation pressure at the local temperature, i.e. $\Psi_p = \Psi_p(P_{sat}(T))$.

On the other hand, the dispersed phase can only exist in equilibrium with the primary one, hence the thermodynamic properties are always expressed as a function of the saturation pressure only, i.e. $\Psi_d = \Psi_d(P_{sat}(T))$.

For both phases, the thermodynamic tables are generated by making use of Refprop®, which implements

(a) Example of LUT discretization (7×7)

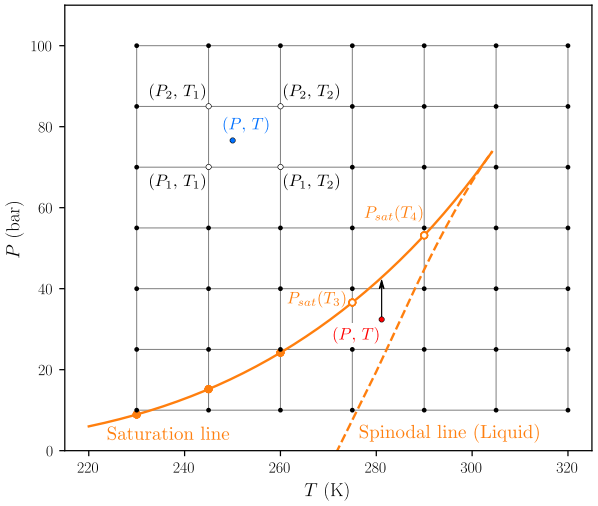

(b) Example of thermodynamic property, $\Psi = \rho$

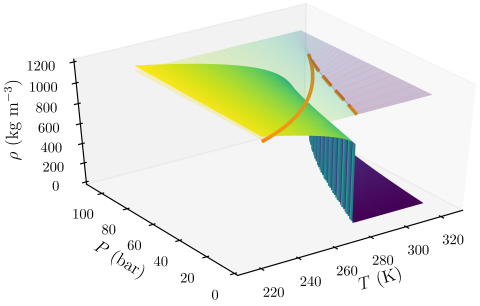

(c) Bilinear Interpolation
$P > P_{sat}(T)$ (cavitation) or $P > P_c$ or $T > T_c$

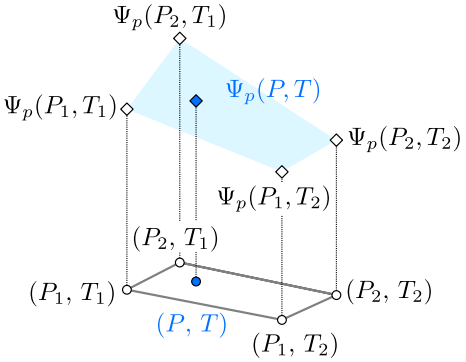

(d) Linear Interpolation
$P \leq P_{sat}(T)$ (cavitation) and $P \leq P_c$ and $T \leq T_c$

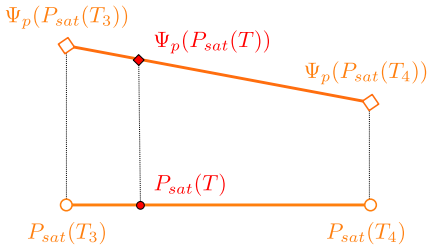

Figure 2:

a multi-parameter equation of state expressed in terms of the Helmholtz fundamental relation [29] for CO_2. Transport properties μ, κ are computed in analogy with the thermodynamic properties, employing the relationships made available by Refprop® in the construction of the tables. The resulting mixture properties follow the averaging procedures described in §2.

2.2. Barotropic model

The set of steady-state governing equations for the barotropic model reads:

$$\begin{aligned} \nabla \cdot (\rho \boldsymbol{v}) &= 0 \\ \nabla \cdot (\rho \boldsymbol{v} \otimes \boldsymbol{v}) &= \nabla \cdot (\mathcal{T} + \mathcal{T}_{turb}) - \nabla P \end{aligned} \tag{9}$$

The two-equation $k - \omega$ SST model [27] completes the system of governing equations by taking into account turbulence effects.

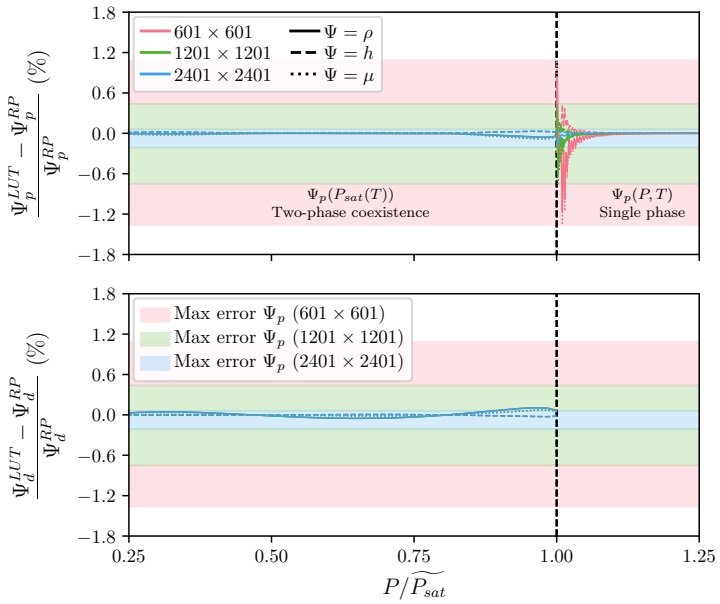

Figure 3:

The barotropic set of equations are simply the single-phase Reynold-Averaged Navier-Stokes equations, in which the fluid behaves like the mixture when the thermodynamic state falls below the saturation curve. Compared to the mixture model, the barotropic formulation inherently excludes any mechanical or thermal disequilibrium between phases, and hence it strictly belongs to the HEM class. Furthermore, the barotropic assumption implies that the thermo-physical properties of the fluid, which should depend on two thermodynamic quantities, are only dependent on pressure, thus neglecting any thermal effect: the fluid is therefore considered compressible but not thermally expandable, i.e. $(\partial\rho/\partial P)_T \neq 0$ and $(\partial\rho/\partial T)_P = 0$ respectively. Such assumption simplifies the resulting flow representation with respect to the classical HEM (whose most general formulation is reported, for example, in [22]), but it provides crucial advantages from the computational perspective. The barotropic model decouples mechanical from thermal effects, removing the need of solving the energy equation to characterize the thermo-physical fluid properties. As a consequence, the mathematical problem is reduced to the resolution of five partial differential equations (for 2D systems), two less than the mixture model. Moreover, the solver becomes inherently more robust than mixture model when dealing with supercritical fluids, because it does not handle the sharp gradients of c_P which arise close to the critical point (wherein c_P is singular). In a hierarchy of CFD models, the barotropic model is therefore the most robust and computationally efficient numerical formulation which can be conceived for tackling the numerical simulation of multi-dimensional two-phase flows of sCO_2.

The physical accuracy of the model strongly relies on the definition of the barotropic relationships for the three thermo-physical properties of interest for the solution, i.e. the density, the molecular viscosity and

the speed of sound c:

$$\rho = \rho(P)$$
$$\mu = \mu(P)$$
$$c = c(P) \tag{10}$$

Since these properties physically depend also on entropy, a choice on the entropy generation across the process has to be made to obtain the three relationships (10). An obvious possibility, considered in the simulations reported in this work, is to keep the entropy level constant at the upstream value $s = s_0$. This choice physically means that the thermal effects prompted by the entropy generation on the aforementioned properties are ignored. It is worth stressing that the choice of building barotropic relationships based on the upstream entropy does not mean to assume isentropic flows: the mechanical dissipation is indeed introduced via viscous and turbulent effects in the momentum equation; the model simply ignores the correction to the thermo-physical properties due to this dissipation, which would cause an increase of entropy. However, if a preliminary estimate on the entropy generation across the process is available, as often occurs for turbocompressor simulations (via the estimated aerodynamic efficiency, for example), the barotropic relations (10) could be in principle constructed considering the estimated entropy rise, thus refining the thermodynamic accuracy of the solution. In the results section we will discuss the contribution given by the entropy generation, by comparing the results of the mixture model with that of the barotropic models.

3. Reference two-phase expanding flows

We here introduce the reference cases against which the two numerical models are validated. Since both the computational strategies focus on the mixture evolution, in principle there should be no differences among cavitating and condensing flows regardless of the phase change initialization. However, despite the generality of the mathematical formulation, the adequacy of the simulation tools in properly representing the macroscopic flow features of two-phase compressible flows has to be verified for both flow conditions. Specifically, we considered the experiments made by Nakagawa *et al.* [30] to validate the computational solver for CO_2 cavitating flows and the experimental data provided by Lettieri *et al.* [7] for the validation of CO_2 condensing flows. For both experiments, the nozzle width is large enough compared to the nozzle height such that three-dimensional effects are expected to be negligible. Therefore, two-dimensional simulations are carried out for both cavitating and condensing flows.

Nakagawa *et al.* [30] analysed cavitating flows of CO_2 for several converging-diverging nozzle geometries, featuring different divergence angles, and for different upstream total conditions. They provided pressure and temperature measurements along the nozzle axis by means of pressure transducers and thermocouples.

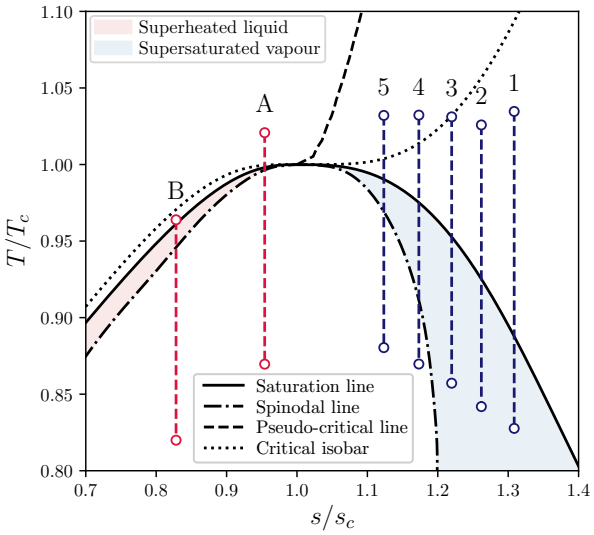

Figure 4: Reference isentropic expansions that are considered in this work for the validation of the proposed computational methodologies.

In the present work, we focused on the nozzle geometry with a divergence angle of 0.153° for the two published upstream total conditions. Based on the isentropic homogeneous theory, the authors claimed that the flow regime is not supersonic for both expansion processes. This conjecture will be object of a specific analysis in the final part of the present paper. Authors also pointed out that a supersonic flow regime was established for nozzle geometries with a higher divergence angle, but the measured pressure falls below the triple point. To avoid dealing with three-phase flows, these latter cases are not considered in this work.

Lettieri *et al.* [7] performed five supersonic expansions at $s > s_c$ whose upstream total state progressively approaches the thermodynamic critical point. They provided the pressure evolution along the nozzle, measured with pressure transducers at several (13) nozzle axial locations; moreover, through an optical apparatus, they also obtained visualizations of the two-phase flows inside the converging-diverging nozzle as well as the experimental condensation onset for each condition. They showed that all expansion processes are characterized by a misty flow regime, where the two phases are practically indistinguishable [7, Fig. 9]. By virtue of such experimental observations, a mixture description of the two-phase flow according to the two-fluid model appears an appropriate approximation.

Table 1 reports the boundary conditions for the cavitating and condensing flows that will be discussed in this work along with the upstream entropy level. Cavitating flows are denoted with a capital letter, while condensing flows are identified by a number. In Figure 4 the corresponding isentropic processes in the T–s thermodynamic plane are reported. Out of the seven conditions available from experiments, case A, case 4 and case 5 are expansions evolving from a supercritical upstream state ($T > T_c$ and $P > P_c$). As a final note,

the shaded areas in Figure 4 represent the extent of the meta-stable region predicted by the multi-parameter equation of state included in the Refprop®. As already stated, in constructing the CFD models the onset of phase change was set at the saturation, thus excluding any meta-stability effects. The plot shows that the extent of the meta-stable regions progressively reduces when approaching the critical point,

Table 1: Summary of boundary conditions for the cavitating (labelled with a capital letter) and condensing (labelled with a number) flows simulated in this work. For condensing flows, the outlet static pressure is not specified because its value is ignored as a consequence of the supersonic flow regime.

Case	P_0^t (bar)	T_0^t (K)	P_1 (bar)	s_0/s_c
A	91.00	310.45	27.5	0.95
B	61.00	293.15	17.5	0.83
1	58.96	314.67	-	1.31
2	65.35	311.99	-	1.26
3	73.53	313.60	-	1.22
4	79.99	313.94	-	1.17
5	84.74	313.88	-	1.12

4. Results

4.1. Cavitating flows

We first consider the case of cavitating flow, occurring when the inlet entropy level is lower than the critical one; such condition is representative of the local expansions occurring in the intake region of the main compressor of sCO_2 closed power cycles [31]. In this context, when the phase transition takes place the primary phase is liquid and the dispersed one is vapour, hence $\alpha_p = \alpha_L$ and $\alpha_d = \alpha_V$. The phase change occurs when $P < P_{sat}(T)$.

Total pressure and total temperature are prescribed at the inlet section as in Table 1 for the two expansion processes considered, imposing $\alpha_V = 0$ therein (the flow enters only in liquid phase). For the barotropic model, only the total pressure is specified. As for the turbulent boundary conditions, a hydraulic diameter equal to 10.0 mm (i.e., twice the height of the inlet section) and an eddy viscosity ratio equal to 2.5 are assigned, representative of a low turbulence level as expected in a nozzle expanding flow from a reservoir; the algorithms implemented in Ansys-Fluent® obtain the corresponding values of k and ω assigned at the inlet. The static pressure is specified at the nozzle outlet as in Table 1. However, it is to be noted that if a supersonic condition is reached at the nozzle outlet, the solver ignores the assigned pressure value and calculates the proper adapted pressure value.

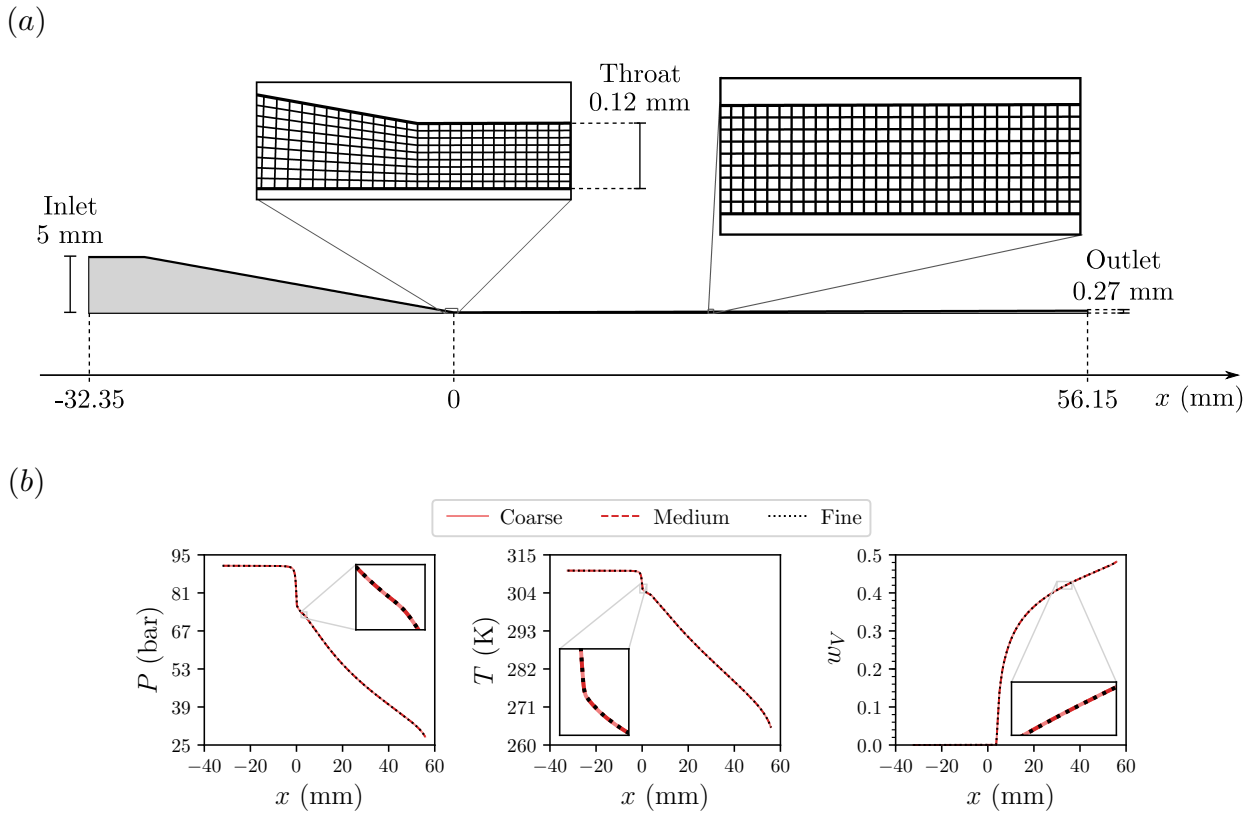

Figure 5:

No-slip and adiabatic boundary conditions are prescribed at the wall, which is not considered smooth. As reported in [32], a mean roughness of 2 µm is considered on the nozzle wall; this value is converted into an equivalent sand-grain roughness using a conversion factor of 3.1 [33], resulting in $k_s = 6.2\,\mu$m. Even though it might appear very small in absolute terms, the relevance of the wall roughness stems from the small scale of the experiment. A comparison with results obtained assuming smooth surfaces will be proposed later in this Section, when discussing the aerodynamics of the nozzle. Finally, a symmetry condition is imposed at the nozzle axis.

The system of equations for the mixture model is solved in the following order: the continuity and the momentum equations are solved together in a coupled fashion, then energy equation, vapour-mass equation and turbulence equations are solved separately in this order. The barotropic model makes use of the same resolution scheme, but energy and vapour-mass equations are not solved. All equations are discretised with a third-order QUICK scheme for both models. Furthermore, the PRESTO! scheme is used to interpolate the pressure at the cell face, while the gradient is reconstructed with a Green-Gauss node-based technique.

A grid convergence assessment is first carried out by generating three hexahedral grids with an increasing number of elements, by taking as a reference the case A. The mixture model is considered for this mesh

Table 2:

	GCI		
x (mm)	P (%)	T (%)	w_V (%)
0	0.01	0.00	0.00
15	0.00	0.00	0.00
30	0.00	0.00	0.00
45	−0.01	0.00	0.00
55	−0.01	0.00	0.00

analysis but equivalent outcomes are found for the barotropic simulations as well. In increasing the mesh resolution, the number of elements are doubled each time in the x-direction while keeping the same wall resolution, i.e. 9 evenly spaced layers in the y-direction with a first-layer wall distance equal to 6.7×10^{-6} m at the throat. The number of elements along the y-direction is dictated by the selected surface roughness, i.e. the first centre-cell distance has to be higher than the roughness value.

The results of this study in terms of main flow distributions is reported in Figure 5, showing that only minor differences are found among three meshes with increasing number of elements. Therefore, the medium mesh is selected for the following analyses, consisting in overall $\approx 3 \times 10^4$ elements, with a grid resolution at throat of 2×10^{-5} m. The selected computational mesh is displayed in Figure 5(a).

As a final and most relevant modeling issue, the setting of the penalty term $\mathcal{G}$ in the mixture model is defined though a set of simulations featuring progressively higher values of the penalty constant $\mathcal{K}$, whose value is raised from $10\,\mathrm{s\,m^{-2}}$ to $10^3\,\mathrm{s\,m^{-2}}$. The results of three calculations are reported in Figure 6 in terms of pressure distributions (left) and vapour mass fraction (right). Simulation results denote an evident convergence process, showing significant differences when the penalty parameter is raised from $10\,\mathrm{s\,m^{-2}}$ to $10^2\,\mathrm{s\,m^{-2}}$, while nearly identical profiles are predicted when $\mathcal{K}$ is raised from $10^2\,\mathrm{s\,m^{-2}}$ to $10^3\,\mathrm{s\,m^{-2}}$. From the results of this analysis, $\mathcal{K} = 10^3\,\mathrm{s\,m^{-2}}$ is systematically set in all following simulations performed with the mixture model.

After the definition of the numerical set-up, we now focus on the experimental assessment of the CFD models. Simulation results are compared against experimental data [30] for both cases A and case B in Figure 7 in terms of pressure and temperature profiles along the nozzle axis.

First considering case A, the agreement between the predicted pressure trends and the experimental one is excellent with both the direct or indirect pressure measurements.

The agreement with the experimental data drops when considering the non-supercritical case B, for that

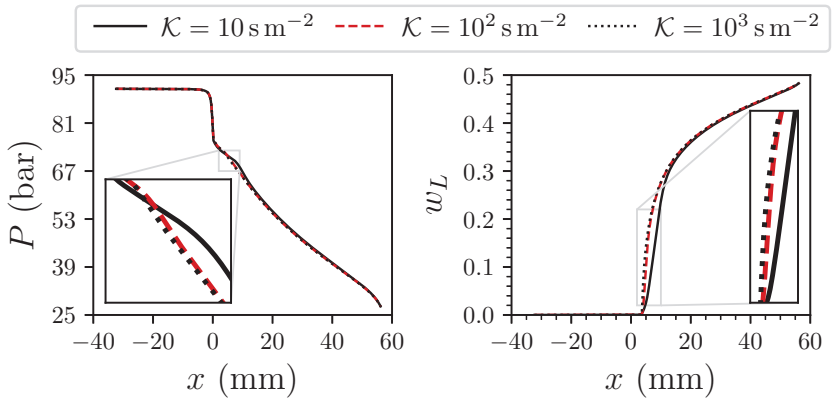

Figure 6: Influence of the penalty constant $\mathcal{K}$ on the solution of the case A.

a systematic over-prediction affects the expansion, although the overall trend is properly reproduced. One possible explanation for such larger deviations is that meta-stable effects, negligible close to the critical point as in case A ($s/s_c = 0.95$), gain importance away from it as in case B ($s/s_c = 0.83$). Such differences are consistent with the results of Palacz *et al.* [22], who also found a reduction in the HEM accuracy away from the critical point. However, a closer inspection of the experimental data for case B shows a certain scattering of the experimental pressure data, especially between direct and temperature-derived measurements.

The above considerations apply identically for both the mixture and the barotropic models, which exhibit qualitatively equal predictions in terms of pressure profiles. However, the thermodynamic implications of the simplified barotropic assumption are interesting to investigate and, hence, a detailed post-processing was performed on the computed data to obtain estimates for:

- the enthalpy field, as $h_{baro} = h(P_0^t, T_0^t) - 0.5 \cdot v_{baro}^2$
- the entropy field, as $s_{baro} = s(P_{baro}, h_{baro})$
- the vapour mass-fraction, as $w_{V,baro} = w_V(P_{baro}, h_{baro})$

These thermodynamic estimates can be performed straightforwardly if the total enthalpy is assumed uniform over the entire flow field. This assumption is actually a simplification of the actual flow configuration: even if the nozzle walls are adiabatic, implying that the flux of total enthalpy must be conserved, local gradients of the total enthalpy might arise as a consequence of internal heat-transfer processes between layers of fluid at different temperature. One classical example is the heat transfer between the boundary layer, heated by the viscous dissipation, and the adjacent free-stream region. The mixture model, by virtue of its complete thermodynamic formulation and its agreement with the experimental temperature profile, can be used as a benchmark for the aforementioned processing of barotropic-simulation data.

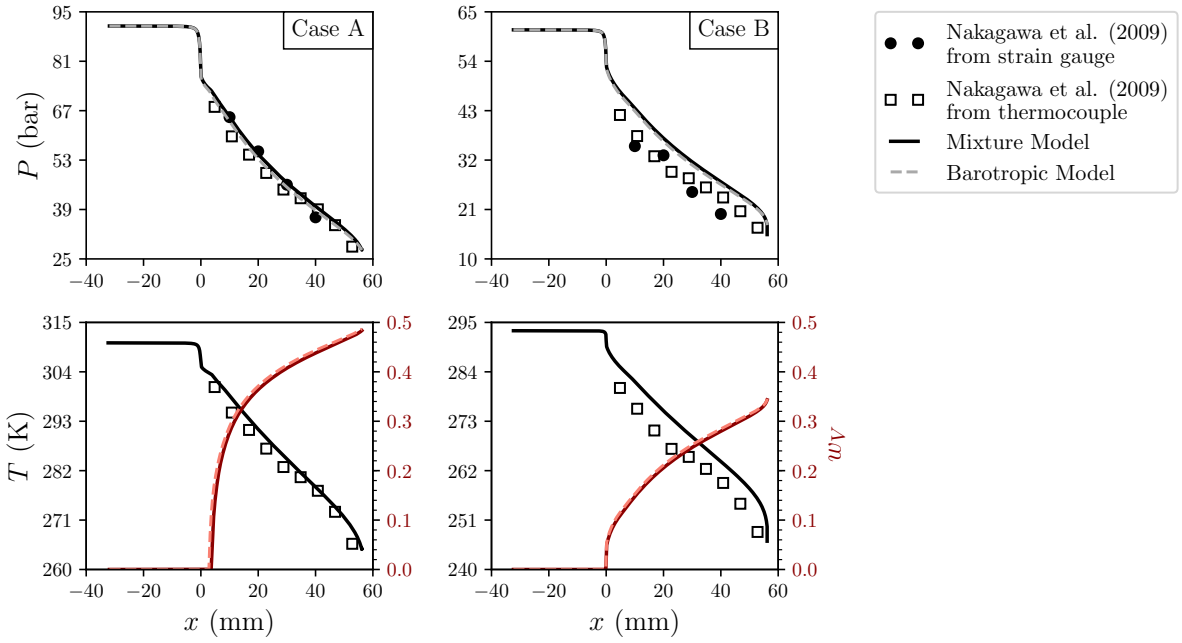

Figure 7: Comparison of the mixture (solid lines) and barotropic (dashed lines) model against experimental data [30] along the nozzle axis. The vapour-mass fraction predicted by the barotropic model is computed as a post-processing.

Figure 8 summarizes significant flow features predicted for the supercritical condition of case A. It reports the two-dimensional distributions of the velocity magnitude, as well as spanwise velocity profiles for three relevant sections across the throat, and the entropy distribution along the nozzle axis. For each of these plots, results obtained with the mixture model (solid lines) are compared with corresponding data extracted/processed from the barotropic flow field (dashed lines). First considering the velocity distributions, it is evident how the two simulation models predict very similar flow configurations in a relatively complex flow field. Indeed, while in the converging region of the nozzle a common configuration is recognized, with a wide isentropic free-stream contoured by a narrow boundary-layer, in the diverging part the isentropic core rapidly vanishes and spanwise gradients affect the entire cross-section, leading to fully-developed profile. By looking at the two-dimensional velocity contours in Figure 8(a) sharp angle at the throat promotes a thickening of the boundary layer, whose dimension rapidly becomes comparable with the nozzle height in the diverging channel, as also confirmed by the spanwise velocity distributions before and after the throat in Figure 8(b).

Such flow field in the diverging part of the nozzle is mostly due to the very low aspect ratio of the duct, but also the very small scale of the experiment plays a role. The diverging duct is indeed so narrow that the wall roughness also significantly contributes to determine the flow configuration. In this work, the surface roughness adopted in [32] is considered, but two further comparative simulations for hydraulically smooth

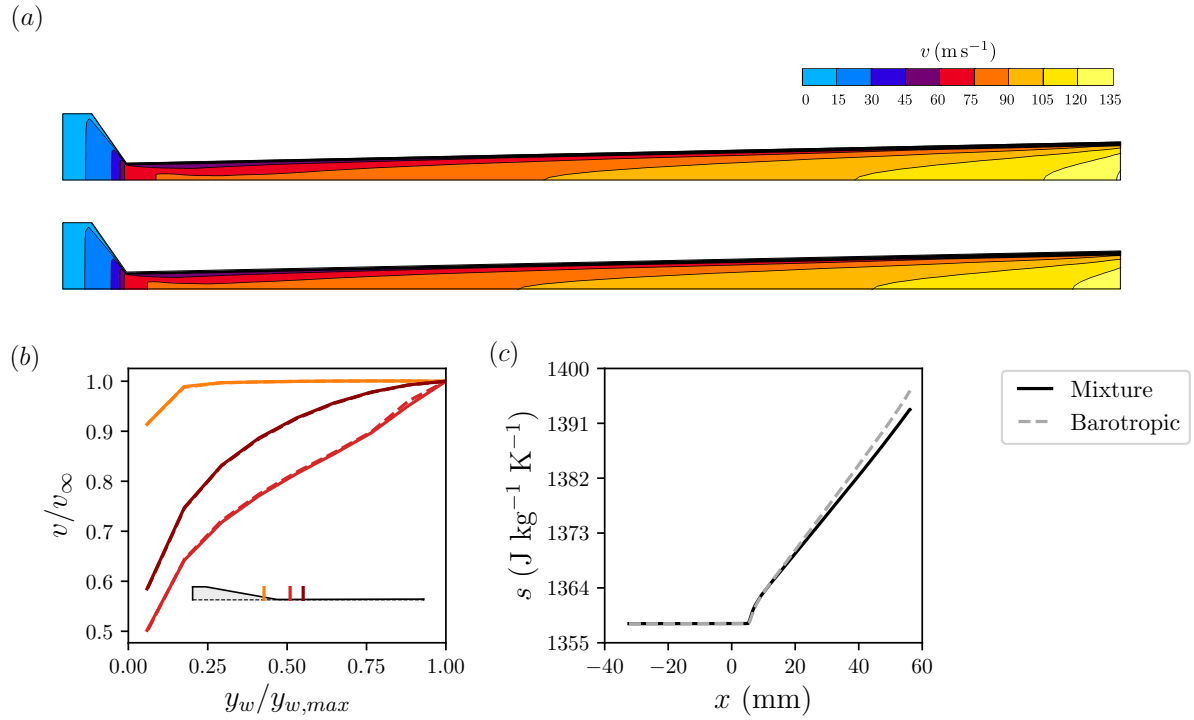

Figure 8: (a) Velocity fields predicted by the mixture model (top) and barotropic model (bottom) for the case A For visualization purposes, the x-direction is stretched such that $x/y = 0.125$ and the convergent section is not shown; (b) spanwise velocity profiles for three relevant sections, namely at $x = -5\,\mathrm{mm}$ (orange lines), 5 mm (red lines) and 10 mm (dark-red lines); (c) entropy distributions along the nozzle axis for the mixture and the barotropic model.

walls were performed. The first one employs the same wall resolution of the rough-wall simulations, and hence resorts to wall-functions for the near-wall treatment, while the second one features a refined mesh clustering at the wall so to achieve $y^+ < 1$ all over the wall boundaries. These two further simulations are compared to the one obtained with rough wall in Figure 9 for both case A and case B. The two smooth-wall simulations show only marginal differences on the pressure profiles (with a slight quantitative differences amplifying towards the nozzle outflow), but they exhibit a considerable difference with respect to the rough-wall simulation, highlighting the significance of the wall roughness in this experiment.

The flow configuration is complex not only on the aerodynamic ground, but also introduces thermodynamic challenges, resulting a very critical benchmark for the present barotropic model, which was constructed by assuming an isentropic pressure-density relation. However, the velocity field reproduced by the barotropic model is aligned with the mixture one , also in the region of developed profiles, where entropy is generated in the boundary layer. Moreover, by inspecting the entropy generation along the nozzle axis, it is evident that the barotropic flow solution, once properly post-processed, can be used to achieve realistic estimates of the mechanical dissipation processes, regardless of the isentropic pressure-density relationship adopted. As a result, when the estimated entropy and the computed pressure are combined to obtain the generation of

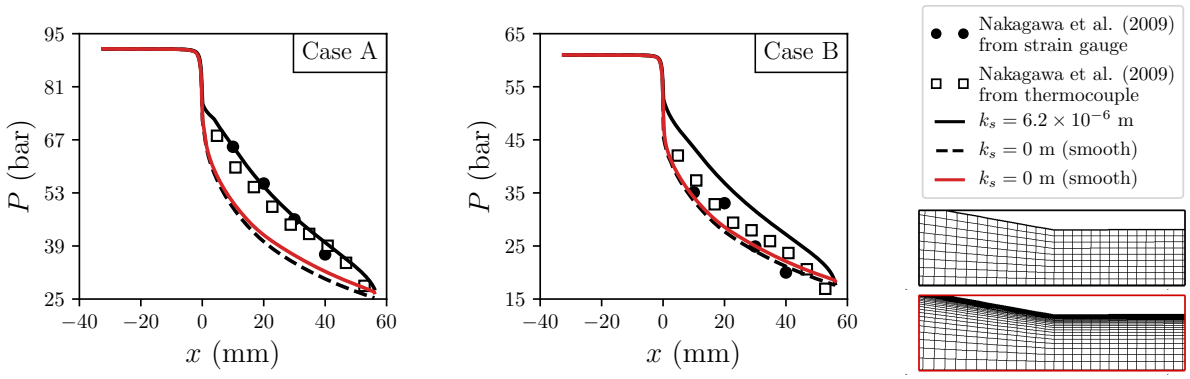

Figure 9:

Table 3:

	Wall functions	$\dot{m}_{mix}$ (kg/s)	$\dot{m}_{baro}$ (kg/s)	$\varepsilon_{mix-baro}$ (%)
		Case A		
Rough wall	✓	4.72	4.80	−1.54
Smooth wall	✓	5.43	5.40	0.59
Smooth wall		5.39	5.36	0.45
		Case B		
Rough wall	✓	3.71	3.77	−1.60
Smooth wall	✓	4.19	4.20	−0.67
Smooth wall		4.16	4.17	−0.33

vapour mass fraction along the nozzle, a remarkable agreement is found between the barotropic model and the complete mixture model, in terms of transition onset, overall trend, and quantitative levels, as visible in Figure 7.

Due to the fully developed profiles observed in the diverging region of the nozzle, the distributions in cross-stream direction are expected to be highly non-uniform for all the quantities, including the vapour mass fraction. The spanwise distributions of w_V at three different axial locations are reported in Figure 10 for case A, showing a consistent increase close to the wall. This can be explained by considering that higher entropy level is found moving away from the nozzle axis, due to the dissipation in the boundary layer. The rise of entropy further increases the vapour quality with respect to that of the flow in the nozzle axis (which is, in turn, higher with respect to the ideal quality in presence of an isentropic expansion). As a result, the vapour-mass fraction at the wall is $3 - 5\%$ higher than the free-stream value. In these trends, slight but

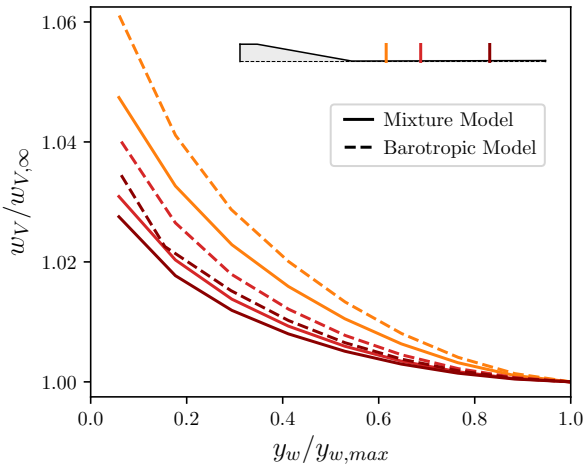

Figure 10: Vapour-mass fraction of case A normalised to the free-stream value at different axial locations, namely at $x = 10\,\text{mm}$ (orange lines), 20 mm (red lines) and 40 mm (dark-red lines).

visible differences appear between the results obtained with the mixture model and with the barotropic one. This is a consequence of the uniform total enthalpy assumption in the post-processing of the barotropic solution: close to the wall, the fluid heated by dissipation exchanges heat with the fluid away from the wall, resulting in a slight reduction of the total enthalpy. This effect, as already noted, cannot be captured in the processing of the barotropic flow solution, which eventually results in a slight overestimate of the enthalpy close to the wall. Consequently, the mass fraction of vapour is slightly overestimated in barotropic estimation, although the discrepancy remains within 1% of the local nozzle-axis value.

The good accuracy of the barotropic flow solution is worth for further physical investigations. As already remarked, the barotropic model implies to consider the fluid compressible but not thermally expandable, i.e. to assume the thermal expansion coefficient $\beta = -\frac{1}{\rho}\left(\frac{\partial \rho}{\partial T}\right)_P$ equal to zero. Figure 11 reports the distribution β for the carbon dioxide in single-phase above saturation, including the liquid, the supercritical and the superheated vapour region. To highlight the effects of thermal expansion, logarithmic scale is used for the contours. The plot indicates that the carbon dioxide is prone to thermal expansion only in a narrow region adjacent to the critical point, where the fluid exhibits severe gradients in all the thermo-physical properties. Among the thermo-physical properties of interest, in the critical region the isobaric heat capacity c_P grows significantly (becoming theoretically infinite at the critical point). The combination of high β and high c_P in the critical region is a further indication of the technical relevance of the barotropic model: where thermal expansion is quantitatively significant, the amount of heat required to alter the fluid temperature is enormous and arguably not comparable with the heating due to viscous dissipation occurring in adiabatic flows.

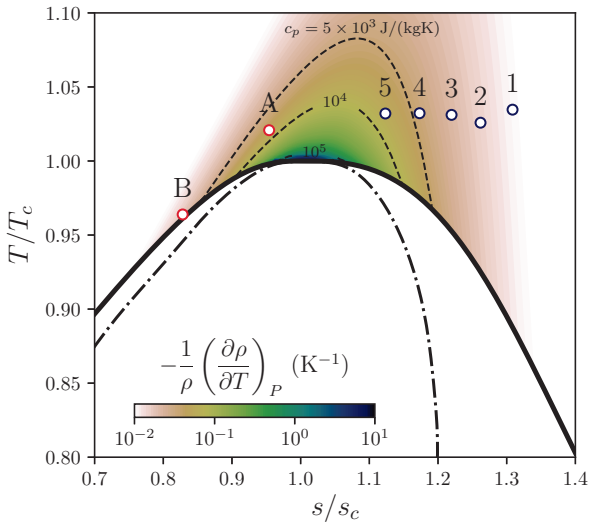

Figure 11: Volumetric coefficient of thermal expansion and isobaric specific heat (black dashed lines) for single-phase CO_2.

4.2. Condensing flows

In condensing flows the primary phase is the vapour phase $\alpha_p = \alpha_V$, while the secondary phase is the liquid phase $\alpha_d = \alpha_L$. The phase change is activated when $P > P_{sat}(T)$.

The computational procedure resembles the one previously described for the cavitating case. Total pressure and total temperature are prescribed at the inlet section as in Table 1 for the five flow configurations, imposing $\alpha_L = 0$ therein (the flow enters only in vapour phase). For the barotropic model, only the total pressure is specified. To impose the typical low turbulence level of a flow expanding from a reservoir, a hydraulic diameter equal to 12.6 mm, i.e. twice the height of the inlet section, and an eddy viscosity ratio equal to 2.5 are assigned as turbulent boundary conditions. As the flow regime is always supersonic, the solver ignores the static pressure value imposed at the outlet. No-slip and adiabatic boundary conditions are prescribed at the wall, while a symmetry condition is imposed at the nozzle axis. Differently from the cavitation experiment, the nozzle used for the condensation study is of sufficiently large scale that the wall is modelled as smooth . The numerical schemes and the solver strategy are identical to the ones already introduced in §4.1.

A grid convergence assessment was carried out by generating three structured meshes with an increasing number of elements. The number of elements was doubled each time in both x- and y-directions while keeping the same wall resolution. Coherently with the smooth-wall condition in combination to the $k-\omega$ SST turbulence model, the near-wall region of the mesh was constructed to avoid the use of wall functions and it is composed by 20 layers in the boundary layer, with a first-layer wall distance equal to 3×10^{-8} m. The maximum $y^+ = 1.2$ is found for the case 5 with three cells within the viscous sub-layer ($y^+ < 10$). The

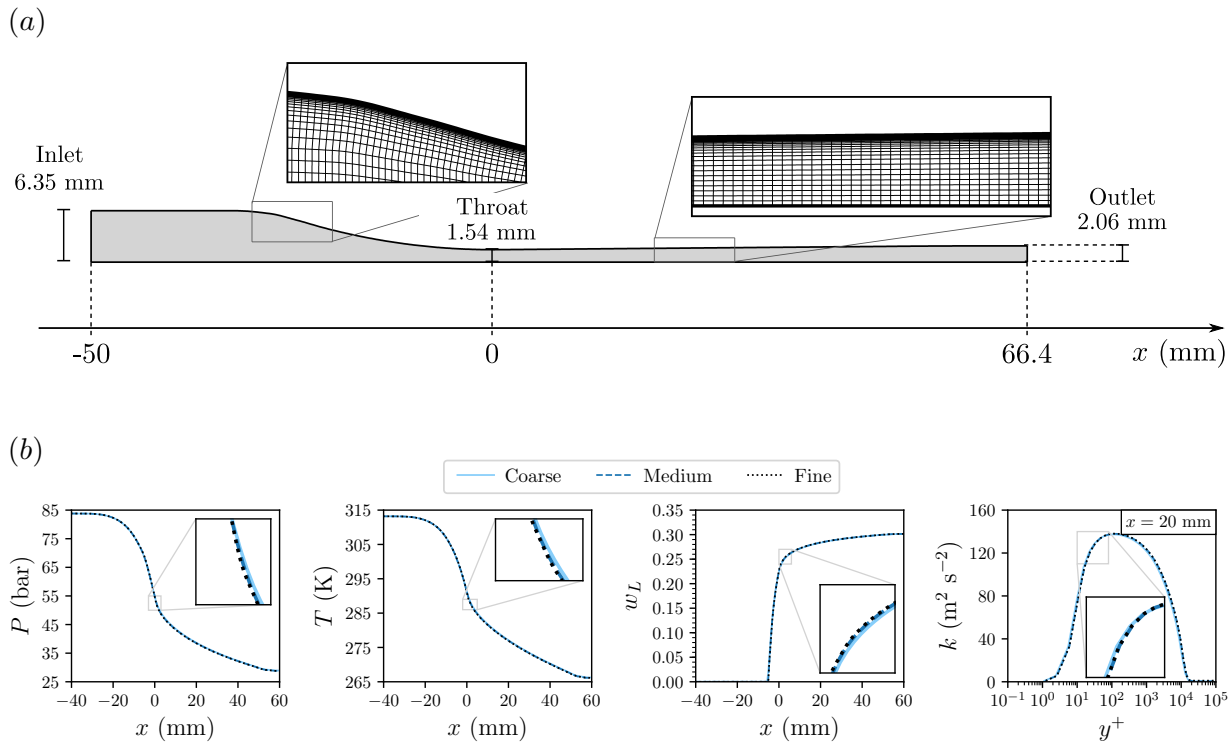

Figure 12:

Table 4:

	GCI		
x (mm)	P (%)	T (%)	w_L (%)
0	0.67	0.12	−2.53
15	0.03	0.00	−0.01
30	0.02	0.00	−0.01
45	0.01	0.00	0.00
60	0.00	0.00	0.00

flow model used in this grid study is the mixture model and we focus on the expansion process closer to the thermodynamic critical point (case 5). Pressure, temperature and liquid-mass fraction trends along the nozzle axis are reported in Figure 12(b) alongside the turbulent kinetic energy distribution at a specified axial location ($x = 20\,\text{mm}$).

Figure 13 reports the comparison of pressure and the liquid-mass fraction distributions against experimental data for the five condensing flows.

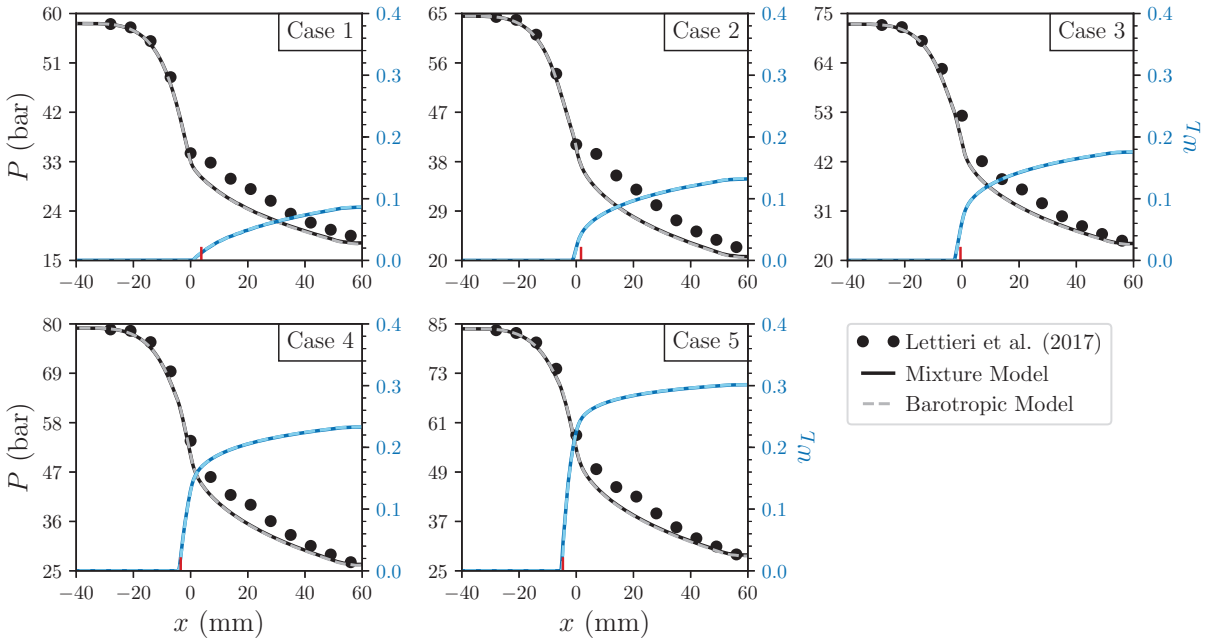

Figure 13:

Table 5:

	$\dot{m}_{mix}$ (kg/s)	$\dot{m}_{baro}$ (kg/s)	$\varepsilon_{mix-baro}$ (%)
Case 1	29.43	29.46	−0.08
Case 2	33.64	33.66	−0.06
Case 3	38.97	38.99	−0.04
Case 4	44.02	44.04	−0.03
Case 5	48.94	48.95	−0.02

When comparing the numerical results to the experiments in Figure 13, the larger pressure discrepancy is found right after the onset of the phase change, where the experimental data exhibit a sudden change in the pressure trend. Furthermore, for the first two cases, an unconventional knee is noticed in the pressure trend close the phase-transition onset, producing a concavity in the pressure trend which remains negative in the first part of the divergent. This feature is not captured by the models, which instead predict a more conventional pressure trend, which smoothly evolves from a negative concavity in the convergent to a positive concavity in the divergent. Such a peculiar trend in the experimental data probably originates from meta-stable equilibrium states, which are expected to be prominent far from the critical point, delaying the

phase transition. Lettieri *et al.* [7] actually identified meta-stability effects in their results, and even derived experimental samples of the Wilson line. They actually found that the largest departure from conventional saturation applies for cases 1 and 2 of the present study

Despite the meta-stability effects discussed above, it is worth highlighting that the present simulation model predicts the condensation onset in a very good approximation for all the cases. In the experiment, the position of transition onset was derived from optical measurement, and it is reported in the frames of Figure 13 as a red tick. In fact, a slight discrepancy is found for the cases far from the critical point (Cases 1 and 2), while a perfect matching is achieved for the expansions from the supercritical state (Cases 4 and 5). This is fully consistent with the above meta-stability effects, but we also note that the experimental identification of condensation point may be affected by a larger uncertainty for Cases 1, 2 and 3. In such cases, the transition is smoother and it is not straightforward to exactly identify the axial location at which the phase change starts, see [7, Fig. 9]. The opposite occurs for the near-critical cases 4 and 5, for that the identification is made easier by the rapid growth of the condensed mass fraction, and the matching with the experiment becomes excellent.

The corresponding mass-fraction flow fields computed by the mixture models are reported in Fig. 14. The flow fields are qualitatively similar to the experimental visualization made by Lettieri *et al.*, in which the condensation location moves back in the nozzle while the upstream thermodynamic state gets closer to the critical point.

5. Mixture speed-of-sound formulation

The two computational models introduced in this work have been shown to reproduce, with a good or acceptable accuracy, the experimental results of compressible two-phase flows, both for cavitation and condensation. Since both models are built on the two-fluid concept, which describes the mixture evolution without detailing the local interfaces between phases, the concept of speed of sound can be extended to the mixture and a 'surrogate' expression for that can be defined.

The definition of the mixture speed of sound is closely linked to the employed two-phase models and its associated assumptions [19, 34]. Moreover, it was demonstrated that the more the system is constrained, the lower the corresponding speed of sound [35, 36]. It means that the HEM speed of sound will be lower than the speed of sound of a HFM, which relaxes the thermal equilibrium assumption. Specifically, the HEM speed of sound is expressed as:

$$c_m^2 = \left(\frac{\partial P}{\partial \rho_m} \right)_s \tag{11}$$

Given the assumptions of the mixture and barotropic model, we expect that this relationship should be used in the determination of the speed of sound and to assess whether or not the flow regime is supersonic.

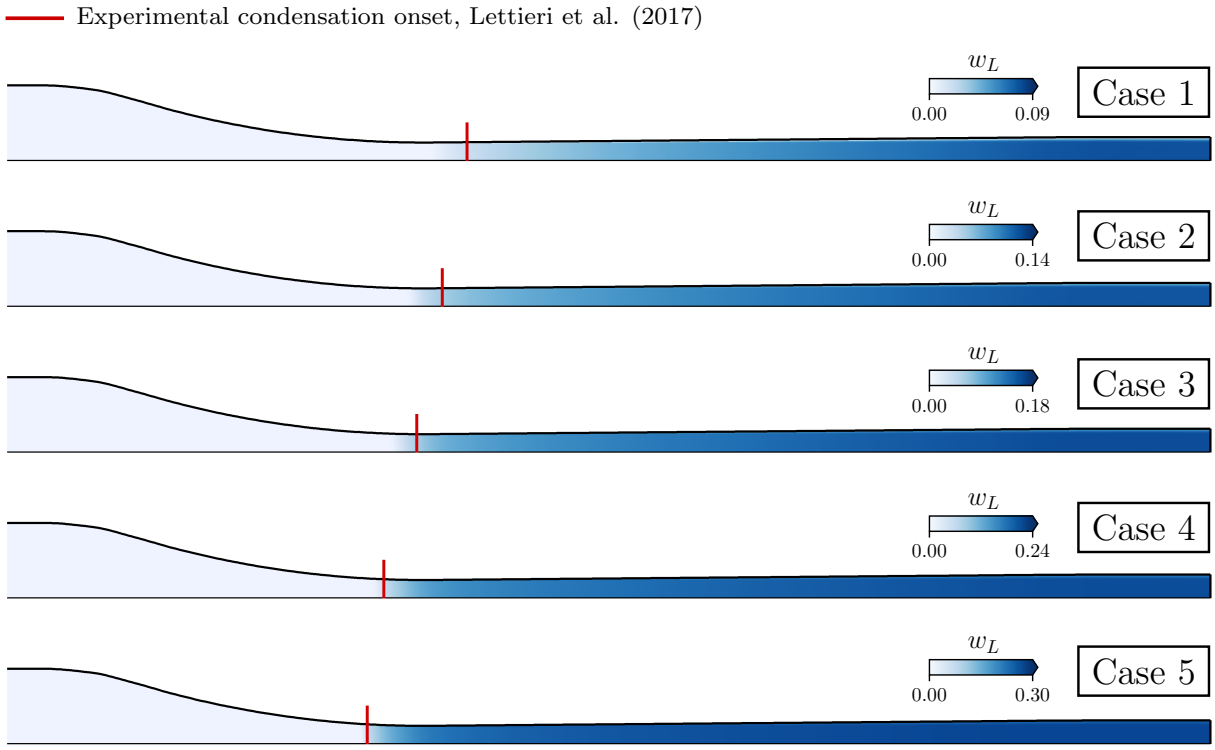

Figure 14: Liquid-mass fraction distributions for the five condensing flows as predicted by the mixture model. The red tick identifies the condensation onset observed experimentally by Lettieri *et al.* [7, Tab. 3]

By default, Ansys-Fluent® makes use of the speed-of-sound formulation :

$$\frac{1}{\rho_m c_m^2} = \frac{\alpha_L}{\rho_L c_L^2} + \frac{\alpha_V}{\rho_V c_V^2} \tag{12}$$

The expression says that the bulk modulus of the mixture $\rho_m c_m^2$ is the harmonic average of the bulk moduli of the components weighted on their volume fractions. In analogy with the analysis of Giacomelli *et al.* [23], we also include the definition of the mixture speed of sound provided by Brennen [17].

$$\frac{1}{\rho_m c_m^2} = \frac{\alpha_V}{P}[(1-\epsilon_V)f_V + \epsilon_V g_V] + \frac{\alpha_L}{P}[(1-\epsilon_L)f_L + \epsilon_L g_L] \tag{13}$$

which considers that a portion of the phases can exchange heat and momentum instantaneously (ϵ_L, ϵ_V), promoting equilibrium, and the remaining portion ($1-\epsilon_L$, $1-\epsilon_V$) does not contribute to the exchange, promoting disequilibrium. In this way, depending on the portion of fluid involved in the phase change, either the HEM ($\epsilon_L = \epsilon_V = 1$) or the HFM ($\epsilon_L = \epsilon_V = 0$) can be recovered. On top of that, Brennen suggested the following approximations: $f_V = g_V \approx 1$, $f_L \approx 0$, $\epsilon_L \approx \alpha_V$, and $g_L \approx 2.1(P/P_c)^{-0.566}$ for carbon dioxide only. Plugging into Eq. (13) the above simplifications, the following expression for the mixture speed of sound is obtained:

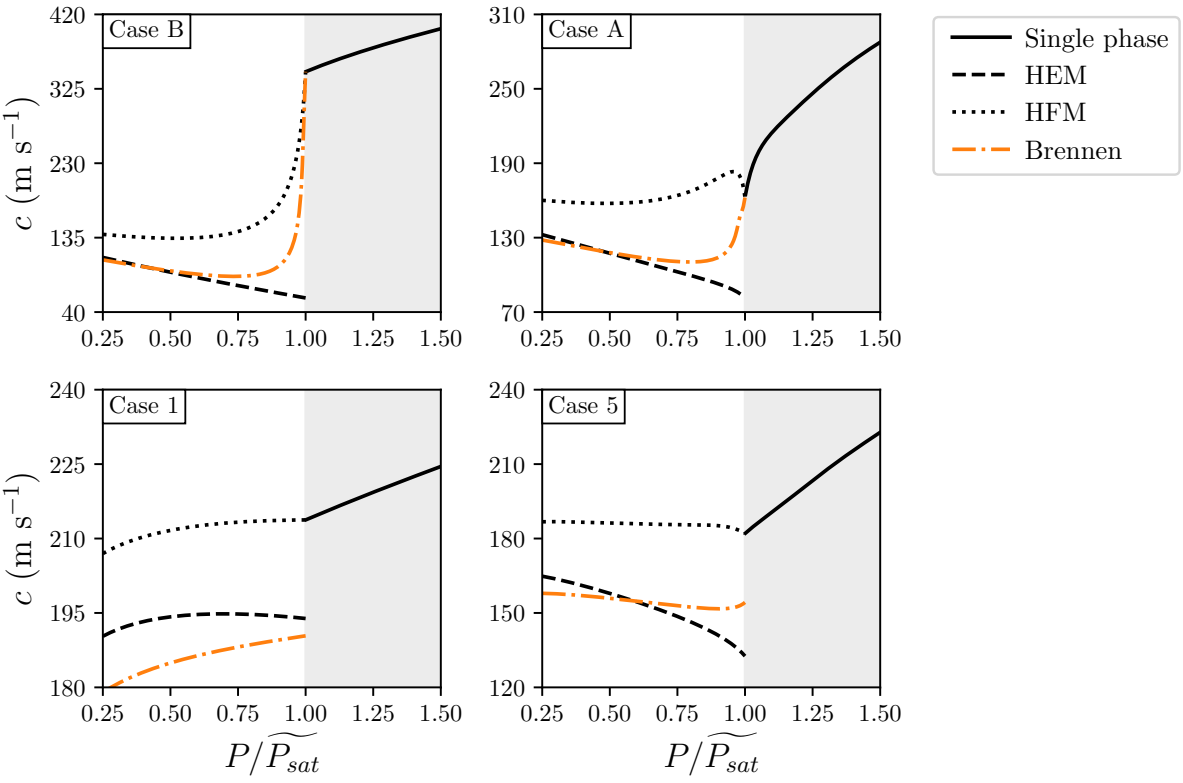

Figure 15: Comparison among different two-phase speed-of-sound formulations: homogeneous equilibrium model (Equation 11), homogeneous frozen model (Equation 12) and an hybrid formulation between the homogeneous equilibrium model and the homogeneous frozen model proposed by Brennen [17] (Equation 14).

$$\frac{1}{\rho_m c_m^2} = 2.1 \frac{\alpha_L \alpha_V}{P^{1.566}} P_c^{0.566} + \frac{\alpha_V}{P} \tag{14}$$

Figure 15 reports the speeds of sound computed according to three expressions (11), (12) and (14) for isentropic expansions of cavitating (case A and B) and condensing (case 1 and 5) flows. The HEM speed of sound exhibits a discontinuity at the saturation [35], which is more pronounced for cavitating flows. Interestingly, the HEM speed of sound generally increases along isentropic expansion (unless case 1, which is far from the critical point and applications of interest) while the single-phase carbon-dioxide speed of sound always decreases along isentropic expansion. Such evidence can be interpreted in terms of the fundamental derivative of the gas dynamics $\Gamma = 1 + \frac{\rho}{c}\left(\frac{\partial c}{\partial \rho}\right)_s$ [37], which is lower than the unity in the two-phase region of carbon dioxide. Moreover, under the HEM assumptions, $\Gamma < 0$ in the near-critical two-phase region [38], paving the way for the occurrence of non-classical effects [39]. It is worth specifying that the expression (14) shows a spike for cavitating flows at the saturation, possibly due to the approximations that were introduced. To avoid this unphysical behaviour, the maximum speed of sound was limited at the single-phase speed of

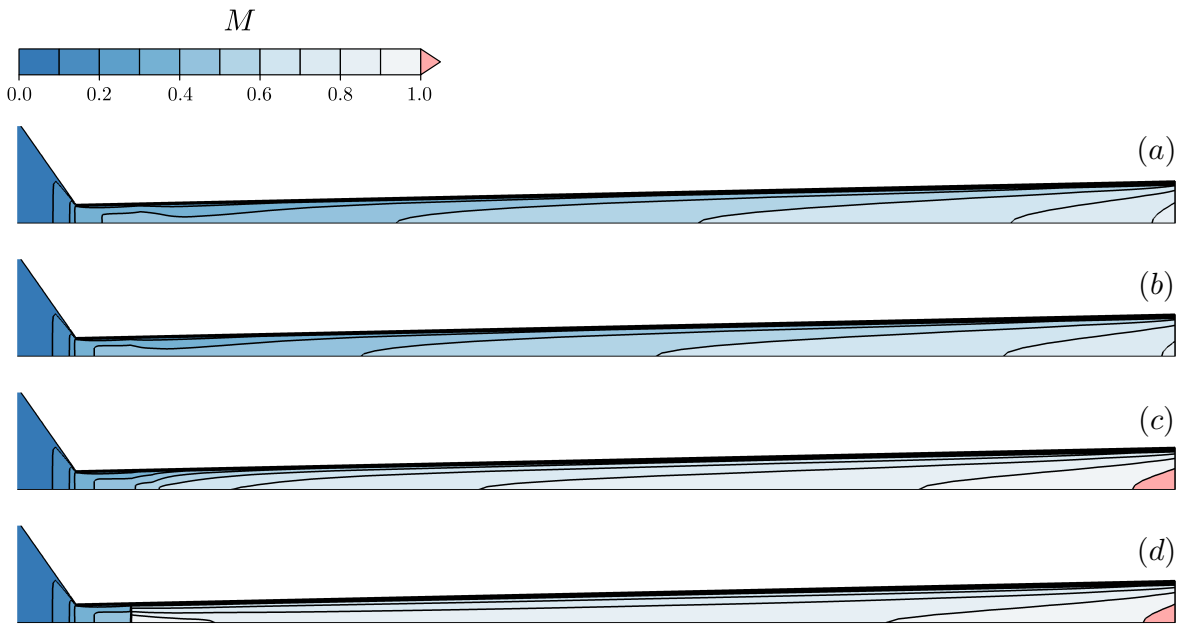

Figure 16: Mach number distributions for the case A (cavitating flow) using different two-phase speed-of-sound formulation: (a) Ansys-Fluent® mixture-model built-in formulation, (b) HFM, (c) Brennen, (d) HEM. For visualization purposes, the x-direction is stretched such that $x/y = 0.125$ and the convergent section is not shown.

sound.

Figure 16 displays the Mach number fields for case A (cavitation). Specifically, Figure 16(a) is the Mach number field as provided by Ansys-Fluent® for the mixture model, while Figures 16(b–d) are obtained by setting the three different speed-of-sound formulations in the equation (10) of the barotropic model. First, the nearly identical distributions obtained in Figure 16(a)–(b) confirms that the present version of Ansys-Fluent® makes use of equation (12) as a post-processing for the mixture speed of sound. As a consequence of the higher speed of sound under HFM assumptions, the Mach number is everywhere lower than unity, reaching the maximum value of $M = 0.82$ at the nozzle outlet. In accordance with Figure 15, the main difference between Figure 16(c)–(d) is located at the phase-transition onset, in which the HEM model predicts a sudden drop. Brennen's formulation instead smears the discontinuity, then recovering approximately the same Mach number evolution predicted by the HEM formulation towards the nozzle outlet, in which a slightly supersonic Mach number ($M = 1.06$) is predicted.

As a final comment, the Mach number field obtained with Brennen's model, which accepts a degree of disequilibrium, do not diverge significantly from solutions obtained with HEM simulation tools. This finding provides a crucial indication on the technical relevance of CFD simulations tools based on the assumption of homogeneous equilibrium for sCO_2 compressor design and analysis, especially when it comes to the

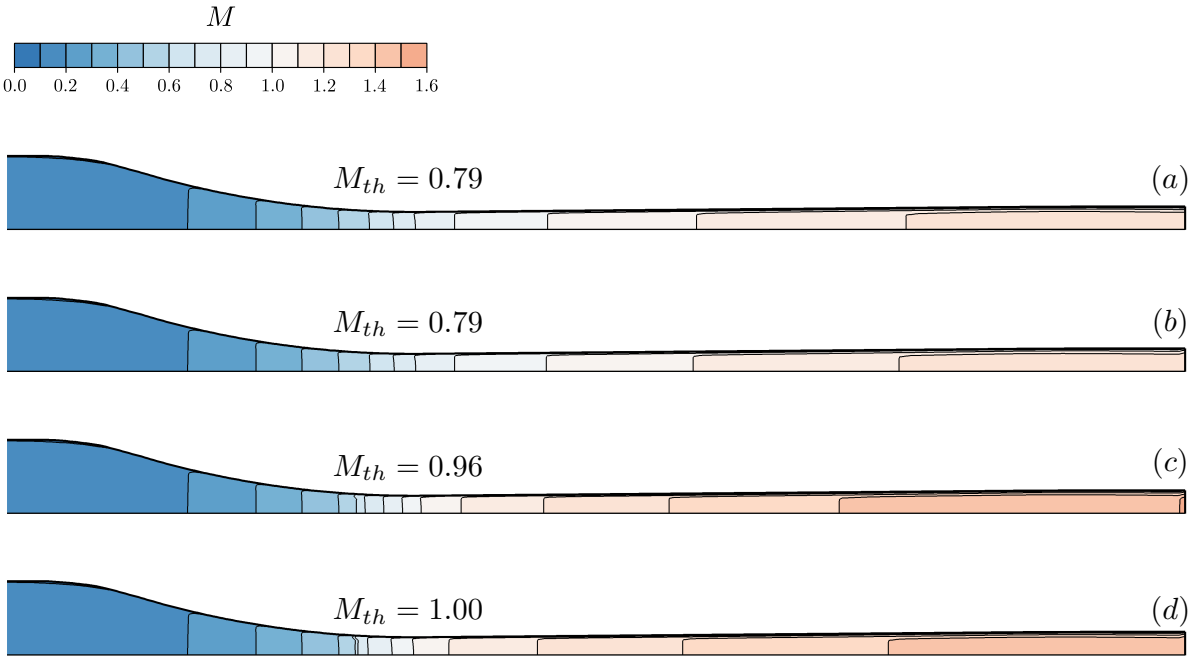

Figure 17: Mach number distributions for the case 5 (condensing flow) using different two-phase speed-of-sound formulation: (*a*) Ansys-Fluent® mixture-model built-in formulation, (*b*) HFM, (*c*) Brennen, (*d*) HEM. The Mach number at the geometrical throat M_{th} is also reported.

identification of the choking limit.

A similar analysis is illustrated in Figure 17 for the case 5 (condensation). Again, the default choice of Ansys-Fluent® , which corresponds to the HFM formulation, provides the lowest Mach number, with the onset of the sonic Mach number after the geometrical throat. Although the sonic throat may be different from the geometrical one when the boundary layer is considered, the streamwise location where the sonic Mach number onsets seems not consistent with the boundary-layer displacement thickness. This observation corroborates the idea that the expression for the speed of sound in (12) is not consistent with the HEM governing equations. On the other hand, the HEM expression (11) predicts a sonic Mach number in the geometrical throat, consistently with the assumptions of the model. As a matter of fact, in presence of mechanical and thermal equilibrium among phases, the single-phase gas dynamics should be theoretically recovered for the mixture.

6. Conclusion

The paper has presented and discussed two computational strategies to simulate compressible two-phase flows of carbon dioxide for industrial applications, operating in the proximity of the thermodynamic critical point and in supercritical conditions. Both models rely on the description of the mixture properties by

resorting to the so-called two-fluid concept, thus eliminating the need of detailing the local interaction between phases. This allows to achieve a considerable simplification in the mathematical modeling, in view of their application to the design and analysis of supercritical carbon dioxide compressors. The first formulation, named *mixture model*, consists in the full-set of governing equations for the mixture plus an additional transport equation that governs the phase transitions; the onset of phase change is driven by the difference between the local pressure and the saturation pressure at the local temperature, by resorting to a penalty formulation. The second formulation, named *barotropic model*, strictly assumes mechanical and thermal equilibrium and the mixture thermo-physical properties are expressed as functions of the pressure only. These simplifications leads to a reduction of the overall computational cost alongside an increased solver robustness, by virtue of the simplified thermodynamic treatment.

The two models have been compared against experiments published in literature for cavitating (liquid $\mapsto$ vapour) and condensing (vapour $\mapsto$ liquid) flows. Both the comparisons involve expansion processes that progressively approach the critical point, where large discrepancies from the ideal-gas thermodynamics are observed. The two models exhibit a remarkable agreement with each other and are able to reproduce the trends set by the experimental data, also showing an overall good quantitative agreement with measured data.

More significant quantitative differences emerge when considering expansions evolving from subcritical states. We conjecture that most of the deviations can be attributed to meta-stable effects, which might delay the phase-change onset in the conditions farthest from the critical point, or to the presence of a relative motion between phases. The mixture model, even though expressed under mechanical and thermal equilibrium in this work, is enough flexible to possibly relax these assumptions via constitutive equations, when detailed experimental data will enable their formulations for compressible flows of carbon dioxide. In the limit of the homogeneous equilibrium approximation, the barotropic model has been shown to provide comparable predictions of the expansion processes at a lower computational cost and with an improved solver robustness.

Appendix A. Tabular results

Table A.6:

$\frac{P_{mix} - P_{baro}}{P_{mix}}$	**Case A** Rough	**Case A** Smooth	**Case B** Rough	**Case B** Smooth	**Case 1**	**Case 2**	**Case 3**	**Case 4**	**Case 5**
Max	2.9%	7.4%	2.3%	7.2%	1.0%	0.9%	0.9%	0.8%	0.9%
Min	0.0%	−0.1%	0.0%	0.0%	0.0%	−0.6%	−0.3%	−0.3%	−0.5%

Table A.7:

	Case A						**Case B**					
	Rough			**Smooth**			**Rough**			**Smooth**		
x (mm)	P_{exp} (bar)	P_{mix} (bar)	ε (%)	P_{exp} (bar)	P_{mix} (bar)	ε (%)	P_{exp} (bar)	P_{mix} (bar)	ε (%)	P_{exp} (bar)	P_{mix} (bar)	ε (%)
10	65.17	65.18	0.0	65.17	50.51	−22.5	35.10	43.54	24.0	35.10	34.17	−2.6
20	55.47	54.70	−1.4	55.47	41.90	−24.5	33.06	36.87	11.5	33.06	28.58	−13.6
30	46.01	46.61	1.3	46.01	36.55	−20.6	24.90	31.60	26.9	24.90	24.99	0.4
40	36.78	39.90	8.5	36.78	32.27	−12.2	20.00	27.17	35.8	20.00	22.10	10.5
	T_{exp} (K)	T_{mix} (K)	ε (%)	T_{exp} (K)	T_{mix} (K)	ε (%)	T_{exp} (K)	T_{mix} (K)	ε (%)	T_{exp} (K)	T_{mix} (K)	ε (%)
4.8	300.61	302.57	0.7	300.61	293.32	−2.4	280.41	285.11	1.7	280.41	277.05	−1.2
10.8	294.93	298.07	1.1	294.93	287.16	−2.6	275.79	281.29	2.0	275.79	271.81	−1.4
16.8	291.06	293.49	0.8	291.06	282.38	−3.0	270.94	277.30	2.3	270.94	267.67	−1.2
22.8	286.90	289.27	0.8	286.90	278.70	−2.9	266.85	273.62	2.5	266.85	264.43	−0.9
28.8	282.81	285.33	0.9	282.81	275.57	−2.6	265.06	270.17	1.9	265.06	261.65	−1.3
34.8	280.55	281.57	0.4	280.55	272.65	−2.8	262.39	266.88	1.7	262.39	259.05	−1.3
40.8	277.52	277.86	0.1	277.52	269.93	−2.7	259.27	263.60	1.7	259.27	256.62	−1.0
46.8	272.84	273.96	0.4	272.84	267.40	−2.0	254.63	260.13	2.2	254.63	254.36	−0.1
52.8	265.72	269.20	1.3	265.72	265.05	−0.3	248.36	255.70	3.0	248.36	252.27	1.6

Table A.8:

	Case 1			**Case 2**			**Case 3**			**Case 4**			**Case 5**		
x (mm)	P_{exp} (bar)	P_{mix} (bar)	ε (%)	P_{exp} (bar)	P_{mix} (bar)	ε (%)	P_{exp} (bar)	P_{mix} (bar)	ε (%)	P_{exp} (bar)	P_{mix} (bar)	ε (%)	P_{exp} (bar)	P_{mix} (bar)	ε (%)
−28	58.08	58.02	0.1	64.38	64.36	0.0	72.44	72.46	0.0	78.77	78.88	0.1	83.47	83.63	0.2
−21	57.48	57.13	−0.6	63.85	63.41	−0.7	71.97	71.44	−0.7	78.46	77.84	−0.8	82.80	82.59	−0.3
−14	54.97	54.38	−1.1	61.14	60.53	−1.0	68.89	68.36	−0.8	75.94	74.70	−1.6	80.49	79.48	−1.3
−7	48.40	47.10	−2.7	54.01	53.08	−1.7	62.67	60.57	−3.3	69.42	66.98	−3.5	74.10	72.05	−2.8
0	34.54	33.08	−4.2	41.12	40.40	−1.8	52.24	46.04	−11.9	53.96	50.68	−6.1	57.99	54.54	−5.9
7	32.82	28.64	−12.7	39.41	33.14	−15.9	42.11	37.84	−10.1	45.90	41.83	−8.9	49.71	45.28	−8.9
14	29.89	26.14	−12.5	35.48	29.97	−15.5	38.11	34.28	−10.1	41.90	37.95	−9.4	45.35	41.17	−9.2
21	28.01	24.20	−13.6	32.91	27.65	−16.0	35.81	31.65	−11.6	39.71	35.09	−11.6	43.03	38.12	−11.4
28	25.87	22.57	−12.8	30.07	25.77	−14.3	32.74	29.53	−9.8	36.07	32.77	−9.1	38.95	35.64	−8.5
35	23.51	21.22	−9.7	27.31	24.20	−11.4	29.84	27.73	−7.1	32.99	30.81	−6.6	35.58	33.55	−5.7
42	21.89	20.03	−8.5	25.28	22.83	−9.7	27.63	26.18	−5.3	30.55	29.10	−4.7	32.90	31.72	−3.6
49	20.59	18.98	−7.8	23.75	21.63	−8.9	25.89	24.80	−4.2	28.63	27.59	−3.6	30.91	30.09	−2.6
56	19.50	18.24	−6.5	22.43	20.78	−7.3	24.39	23.84	−2.3	26.92	26.53	−1.5	28.98	28.94	−0.1

Nomenclature

Acronyms

CCS	carbon-capture sequestration
CFD	computational fluid dynamic
DEM	deleyed equilibrium model
GCI	grid convergence index
HEM	homogeneous equilibrium model
HFM	homogeneous frozen model
LUT	look-up table
NEM	non-homogeneous equilibrium model
sCO_2	supercritical carbon dioxide
UDF	user-defined function
UDRGM	user-defined real-gas model
WMAPE	weighted mean absolute percentage error

Greek Symbols

α	volume fraction	$[-]$
β	thermal expansion coefficient	$[\mathrm{K}^{-1}]$
ϵ	interacting fluid portion	$[-]$
Γ	fundamental derivative of gas dynamics	$[-]$
κ	thermal conductivity	$[\mathrm{W\,m^{-1}\,K^{-1}}]$
μ	dynamic viscosity	$[\mathrm{Pa \cdot s}]$
Ψ	thermodynamic/transport property	
ψ	specific thermodynamic property	
ρ	density	$[\mathrm{kg\,m^{-3}}]$

Roman Symbols

c	speed of sound	$[\mathrm{m\,s^{-1}}]$
c_P	specific isobaric heat capacity	$[\mathrm{J\,kg^{-1}\,K^{-1}}]$
f, g	Brennen's thermodynamic functions	$[-]$
$\mathcal{G}$	phase-change source term	$[\mathrm{kg\,m^{-3}\,s^{-1}}]$
h	mass-specific enthalpy	$[\mathrm{J\,kg^{-1}}]$
k	turbulent kinetic energy	$[\mathrm{m^2\,s^{-2}}]$
$\mathcal{K}$	penalty constant	$[\mathrm{s\,m^{-2}}]$
k_s	sand-grain roughness	[m]
M	Mach number	$[-]$
$\dot{m}$	mass-flow rate	$[\mathrm{kg\,s^{-1}}]$
P	pressure	[Pa]
$\widetilde{P_{sat}}$	saturation pressure at the upstream entropy	[Pa]
P_{sat}	saturation pressure at the local temperature	[Pa]
q	heat flux	$[\mathrm{W\,m^{-2}}]$
q_{turb}	turbulent heat flux	$[\mathrm{W\,m^{-2}}]$
s	mass-specific entropy	$[\mathrm{J\,kg^{-1}\,K^{-1}}]$
T	temperature	[K]
$\mathcal{T}$	stress tensor	[Pa]
$\mathcal{T}_{turb}$	Reynolds stress tensor	[Pa]
v	velocity	$[\mathrm{m\,s^{-1}}]$
w	mass fraction	$[-]$
x	axis direction	[m]
y	span direction	[m]

y^+	dimensionless wall distance	[–]

Subscripts and superscripts

0	nozzle inlet
1	nozzle outlet
∞	free-stream
baro	barotropic model
c	thermodynamic critical point
d	dispersed/secondary phase
exp	experimental value
L	liquid phase
m	mixture property
max	maximum value
mix	mixture model
p	primary phase
sat	saturation property
t	total quantity
th	nozzle throat
V	vapour phase
w	wall

References

[1] G. Lorentzen, Revival of carbon dioxide as a refrigerant, International Journal of Refrigeration 17 (5) (1994) 292 – 301. doi:10.1016/0140-7007(94)90059-0.

[2] S. Elbel, N. Lawrence, Review of recent developments in advanced ejector technology, International Journal of Refrigeration 62 (2016) 1 – 18. doi:10.1016/j.ijrefrig.2015.10.031.

[3] G. Angelino, Carbon Dioxide Condensation Cycles For Power Production, Journal of Engineering for Power 90 (3) (1968) 287–295. doi:10.1115/1.3609190.

[4] E. Feher, The supercritical thermodynamic power cycle, Energy Conversion 8 (2) (1968) 85 – 90. doi:10.1016/0013-7480(68)90105-8.

[5] V. Dostal, A supercritical carbon dioxide cycle for next generation nuclear reactors, Ph.D. thesis, Massachusetts Institute of Technology (2004).

[6] F. Crespi, G. Gavagnin, D. Sanchez, G. S. Martinez, Supercritical carbon dioxide cycles for power generation: A review, Applied Energy 195 (2017) 152–183. doi:10.1016/j.apenergy.2017.02.048.

[7] C. Lettieri, D. Paxson, Z. Spakovszky, P. Bryanston-Cross, Characterization of Nonequilibrium Condensation of Supercritical Carbon Dioxide in a de Laval Nozzle, Journal of Engineering for Gas Turbines and Power 140 (4) (2017) 041701. doi:10.1115/1.4038082.

[8] Y. Bartosiewicz, Modeling of two-phase choked flows, in: S. Chabane, J.-M. Buchlin (Eds.), Flow Characteristics and performance of safety valves. Lecture Series 2013-08, Von Karman Institute for Fluid Dynamics, 2013.

[9] D. Tan, Y. Li, I. Wilkes, E. Vagnoni, R. L. Miorini, J. Katz, Experimental investigation of the role of large scale cavitating vortical structures in performance breakdown of an axial waterjet pump, Journal of Fluids Engineering 137 (111301) (2015). doi:10.1115/1.4030614.

[10] R. Diener, J. Schmidt, Sizing of throttling device for gas/liquid two-phase flow Part 1: Safety valves, Process Safety Progress 23 (2004) 335–344. doi:10.1002/prs.10034.

[11] R. Diener, J. Schmidt, Sizing of throttling device for gas/liquid two-phase flow Part 2: Control valves, orifices, and nozzles, Process Safety Progress 24 (2005) 29–37. doi:10.1002/prs.10035.

[12] A. Hosangadi, V. Ahuja, Numerical Study of Cavitation in Cryogenic Fluids , Journal of Fluids Engineering 127 (2) (2005) 267–281. doi:10.1115/1.1883238.

[13] J. Zhu, S. Wang, X. Zhang, Influences of thermal effects on cavitation dynamics in liquid nitrogen through venturi tube, Physics of Fluids 32 (1) (2020) 012105. doi:10.1063/1.5132591.

[14] J. B. Young, Two-dimensional, nonequilibrium, wet-steam calculations for nozzles and turbine cascades, Journal of Turbomachinery 114 (1992) 569–579. doi:10.1115/1.2929181.

[15] M. Grübel, J. Starzmann, M. Schatz, T. Eberle, D. Vogt, F. Sieverding, Two-Phase Flow Modeling and Measurements in Low-Pressure Turbines - Part I: Numerical Validation of Wet Steam Models and Turbine Modeling, Journal of Engineering for Gas Turbines and Power 137 (042602) (2015). doi:10.1115/1.4028468.

[16] M. Schatz, T. Eberle, M. Grübel, J. Starzmann, D. Vogt, N. Suerken, Two-Phase Flow Modeling and Measurements in Low-Pressure Turbines - Part II: Turbine Wetness Measurement and Comparison to Computational Fluid Dynamics-Predictions, Journal of Engineering for Gas Turbines and Power 137 (042603) (2015). doi:10.1115/1.4028547.

[17] C. E. Brennen, Homogeneous flows, in: Fundamentals of Multiphase Flow, Cambridge University Press, 2005, pp. 176—-198. doi:10.1017/CBO9780511807169.010.

[18] G. Gyarmathy, Nucleation of steam in high-pressure nozzle experiments, Proceedings of the Institution of Mechanical Engineers, Part A: Journal of Power and Energy 219 (6) (2005) 511–521. doi:10.1243/095765005X31388.

[19] M. De Lorenzo, P. Lafon, J.-M. Seynhaeve, Y. Bartosiewicz, Benchmark of delayed equilibrium model (dem) and classic two-phase critical flow models against experimental data, International Journal of Multiphase Flow 92 (2017) 112 – 130. doi:10.1016/j.ijmultiphaseflow.2017.03.004.

[20] Y. Bartosiewicz, Z. Aidoun, Y. Mercadier, Numerical assessment of ejector operation for refrigeration applications based on cfd, Applied Thermal Engineering 26 (5-6) (2006) 604–612. doi:10.1016/j.applthermaleng.2005.07.003.

[21] Q. Dang Le, R. Mereu, G. Besagni, V. Dossena, F. Inzoli, Computational Fluid Dynamics Modeling of Flashing Flow in Convergent-Divergent Nozzle, Journal of Fluids Engineering 140 (10), 101102 (05 2018). doi:10.1115/1.4039908.

[22] M. Palacz, J. Smolka, A. Fic, Z. Bulinski, A. J. Nowak, K. Banasiak, A. Hafner, Application range of the HEM approach for CO2 expansion inside two-phase ejectors for supermarket refrigeration systems, International Journal of Refrigeration

59 (2015) 251 – 258. doi:10.1016/j.ijrefrig.2015.07.006.

[23] F. Giacomelli, F. Mazzelli, A. Milazzo, A novel cfd approach for the computation of r744 flashing nozzles in compressible and metastable conditions, Energy 162 (2018) 1092 – 1105. doi:10.1016/j.energy.2018.08.050.

[24] A. Hosangadi, Z. Liu, T. Weathers, V. Ahuja, J. Busby, Modeling Multiphase Effects in CO2 Compressors at Subcritical Inlet Conditions, Journal of Engineering for Gas Turbines and Power 141 (8) (03 2019). doi:10.1115/1.4042975.

[25] J. Bodys, J. Smolka, M. Palacz, M. Haida, K. Banasiak, Non-equilibrium approach for the simulation of co2 expansion in two-phase ejector driven by subcritical motive pressure, International Journal of Refrigeration 114 (2020) 32 – 46. doi:10.1016/j.ijrefrig.2020.02.015.

[26] M. Ishii, T. Hibiki, Thermo-Fluid Dynamics of Two-Phase Flow, Springer-Verlag New York, 2011. doi:10.1007/978-1-4419-7985-8.

[27] F. R. Menter, Two-equation eddy-viscosity turbulence models for engineering applications, AIAA Journal 32 (8) (1994) 1598–1605. doi:10.2514/3.12149.

[28] J. Young, The condensation and evaporation of liquid droplets in a pure vapour at arbitrary knudsen number, International Journal of Heat and Mass Transfer 34 (7) (1991) 1649 – 1661. doi:10.1016/0017-9310(91)90143-3.

[29] R. Span, W. Wagner, A new equation of state for carbon dioxide covering the fluid region from the triple-point temperature to 1100 k at pressures up to 800 mpa, Journal of Physical and Chemical Reference Data 25 (6) (1996) 1509–1596. doi:10.1063/1.555991.

[30] M. Nakagawa, M. S. Berana, A. Kishine, Supersonic two-phase flow of CO_2 through converging–diverging nozzles for the ejector refrigeration cycle, International Journal of Refrigeration 32 (6) (2009) 1195–1202. doi:10.1016/j.ijrefrig.2009.01.015.

[31] G. Persico, P. Gaetani, A. Romei, L. Toni, E. Bellobuono, R. Valente, Implications of phase change on the aerodynamics of centrifucal compressors for supercritical carbon dioxide applications, in: Proceedings of the ASME Turbo Expo 2020, no. GT2020-14988, 2020, pp. 1–12. doi:10.1115/GT2020-14988.

[32] K. Banasiak, A. Hafner, Mathematical modelling of supersonic two-phase R744 flows through converging–diverging nozzles: The effects of phase transition models, Applied Thermal Engineering 51 (1) (2013) 635 – 643. doi:10.1016/j.applthermaleng.2012.10.005.

[33] T. Adams, C. Grant, H. Watson, A simple algorithm to relate measured surface roughness to equivalent sand-grain roughness, nternational Journal of Mechanical Engineering and Mechatronics 1 (2012) 66–71. doi:10.11159/ijmem.2012.008.

[34] M. De Lorenzo, P. Lafon, M. Di Matteo, M. Pelanti, J.-M. Seynhaeve, Y. Bartosiewicz, Homogeneous two-phase flow models and accurate steam-water table look-up method for fast transient simulations, International Journal of Multiphase Flow 95 (2017) 199 – 219. doi:10.1016/j.ijmultiphaseflow.2017.06.001.

[35] T. Flatten, H. Lund, Relaxation two-phase flow models and the subcharacteristic condition, Mathematical Models and Methods in Applied Sciences 21 (12) (2011) 2379–2407. doi:10.1142/S0218202511005775.

[36] M. Pelanti, K. Shyue, A numerical model for multiphase liquid–vapor–gas flows with interfaces and cavitation, International Journal of Multiphase Flow 113 (2019) 208 – 230. doi:10.1016/j.ijmultiphaseflow.2019.01.010.

[37] P. A. Thompson, A fundamental derivative in gasdynamics, Physics of Fluids 14 (9) (1971) 1843–1849. doi:10.1063/1.1693693.

[38] N. R. Nannan, A. Guardone, P. Colonna, On the fundamental derivative of gas dynamics in the vapor–liquid critical region of single-component typical fluids, Fluid Phase Equilibria 337 (2013) 259–273. doi:10.1016/j.fluid.2012.09.017.

[39] P. A. Thompson, K. C. Lambrakis, Negative shock waves, Journal of Fluid Mechanics 60 (1973) 187–208. doi:10.1017/S002211207300011X.